



22 mm/s to 2150 mm/s. It was found that the bond-slip properties showed remarkable  
23 dynamic enhancing effect under high loading rate (above 800 mm/s). However, at the  
24 loading rate around 2000 mm/s, dynamic effect could be limited by CFRP load capacity  
25 in which the CFRP sheet might directly fractured rather than debonded from the  
26 concrete surface. The effect of parameters on the bond behaviour was better understood  
27 from a detailed experimental parametric study. Constitutive equations were proposed  
28 to model the dynamic bond-slip behaviour of the CFRP-concrete interface.

29

30 *Keywords:* CFRP; concrete; debonding; dynamic tests; peak bond stress; interfacial  
31 fracture energy; parametric study; dynamic increase factor.

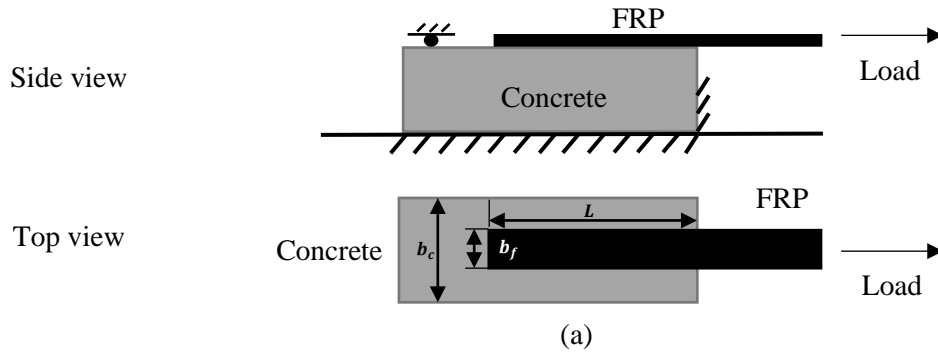
## 32 **1. Introduction**

33 External bonding of fibre reinforced polymer (FRP) has been widely used as an  
34 effective technique for strengthening reinforced concrete (RC) structures [1]. The  
35 effectiveness of this method primarily depends on the interfacial shear bond behaviour  
36 between the FRP and the concrete substrate. To aid the FRP strengthening design in  
37 quasi-static scenarios, shear bond behaviour has been extensively studied through  
38 single-lap and double-lap shear tests under quasi-static loading rates [1-5], as shown in  
39 Figs. 1(a) and 1(b), respectively. In these studies, specimens commonly failed due to  
40 concrete substrate cracking at a layer a few millimetres below the FRP-concrete  
41 interface. Consequently, concrete strength  $f'_c$  significantly influences bonding  
42 behaviour and load-carrying capacity of specimens. The effect of FRP was also  
43 evaluated. Specimens with a greater FRP stiffness ( $E_f t_f$ ) require a greater load to reach

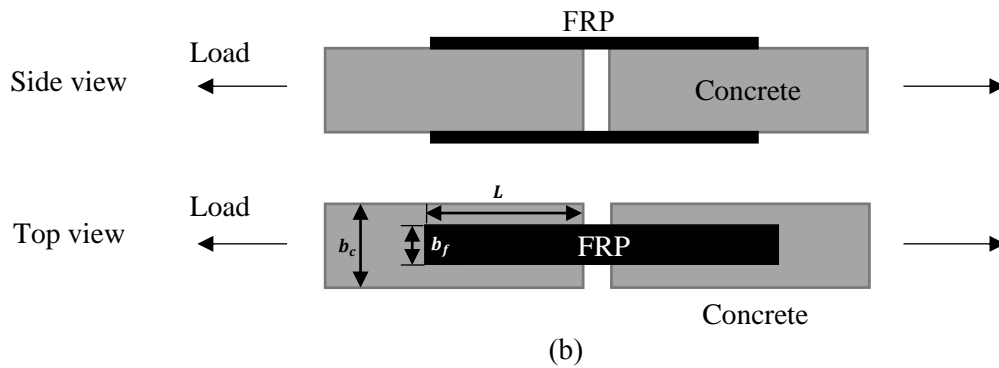
44 the same deformations compared to those with a smaller stiffness. Therefore, for the  
45 same failure strain, load-carrying capacities of specimens with higher FRP stiffness are  
46 significantly greater. Apart from the material properties, FRP bond width and bond  
47 length also affect the interfacial bond properties and the load-carrying capacity [1-3, 5].  
48 Chen and Teng [2] investigated different FRP bond widths  $b_f$  and incorporated a bond  
49 width coefficient  $\beta_w$  to predict the width effect due to different widths of FRP and  
50 concrete substrate ( $b_f$  and  $b_c$ ). From researchers investigating the FRP-concrete bond  
51 length  $L$  [1, 2, 5], it was found that any increase in bond length beyond the effective  
52 bond length  $L_e$  would not improve the load-carrying capacity. This behaviour was  
53 later validated by Cottone and Giambanco [5] in their theoretical study. Accordingly,  
54 Chen and Teng [2] also proposed an equation to predict the effective bond length.

55

56 In summary, four main parameters govern the load-carrying capacity and the bond-slip  
57 behaviour of FRP strengthened concrete in quasi-static tests, namely, FRP stiffness  
58  $E_f t_f$ , the width and length of the FRP-concrete bonding interface ( $b_f$  and  $L$ ) and the  
59 concrete strength  $f'_c$ . Based on numerous tests and analytical studies, some equations  
60 were developed to predict the load-carrying capacity and bond stress-slip relationship  
61 in quasi-static loading regimes [2, 3]. The influence of much softer epoxy has been  
62 investigated by Shi et al. [6]. As normal epoxy was used in the current study and most  
63 references, the effect of softer epoxy was not discussed here. Moreover, an ultrasonic  
64 technique has been applied by La Malfa Ribolla et al. [7] to detect debonding of FRP  
65 from concrete substrate.



66



67

68 Fig. 1. Schematic diagrams of (a) single-lap shear test and (b) double-lap shear test

69

70 In blast tests, the FRP strengthening system helped to reduce deflection and spalling at  
 71 the rear face of RC structures [8-10]. Due to impulsive nature of impact or blast loading,  
 72 the response of the FRP-concrete interface is not the same as that observed under quasi-  
 73 static regime. Orton et al. [11] mentioned that the strain rate reached by the FRP  
 74 material on strengthened RC structures in close-in blast loading was about  $8 \text{ s}^{-1}$ . To  
 75 achieve this strain rate in dynamic shear tests, loading rates of over 800 mm/s need to  
 76 be applied for a 100 mm FRP bond length. It should be noted that, the dynamic bond-  
 77 slip behaviour has not been as well investigated as the quasi-static loading cases. This  
 78 lack of knowledge would limit the accuracy of high-fidelity numerical simulations and  
 79 design of FRP strengthening under impact or blast loading regime.

80

81 Only a few experiments have been carried out to study the dynamic shear debonding  
82 failure of FRP-concrete interface under relatively low loading rates. Shi et al. [12]  
83 investigated the effects of FRP material and concrete strength for loading rates below  
84 20 mm/s with a servo-hydraulic test machine. However, FRP geometric parameters  
85 such as  $b_f$  and  $L$  were not included in their studies. Shen et al. [13] increased the  
86 loading rate to 70 mm/s but no material and geometric parameter was considered.  
87 Additionally, Caggiano et al. [14] proposed an interface model to simulate the dynamic  
88 debonding behaviour of FRP-concrete interface at loading rates from 0.07 to 70 mm/s.  
89 Pereira and Lourenco [15] used a drop weight to apply impact loads on glass fibre  
90 reinforced polymer (GFRP)-masonry specimens. However, they did not use a concrete  
91 substrate in their study. In addition, majority of tests achieved were lower than 800  
92 mm/s. To the authors' best knowledge, shear bond-slip behaviour of FRP-concrete  
93 interface with a much higher loading rate of up to 2000 mm/s has not been reported.  
94 Therefore, in this work a novel experimental method for high loading-rate tests using a  
95 modified Split Hopkinson Pressure Bar (SHPB) set-up was carried out. Due to limited  
96 space in the experimental set-up at Nanyang Technological University (NTU)  
97 protective engineering laboratory, single-lap shear test (Fig. 1(a)) was chosen.  
98 Additionally, CFRP was selected among the different types of FRP for its light weight,  
99 large stiffness and high strength, as well as its wide applications in FRP strengthened  
100 RC structures [8, 9].

101

102 To comprehensively study the CFRP dynamic debonding behaviour, the present  
103 programme investigated the dynamic enhancing effect of CFRP-concrete bond ranging  
104 from quasi-static to high loading rates (0.02 mm/s to about 2000 mm/s). It is noteworthy  
105 that when considering the physical debonding process, slip rate is the practical  
106 debonding velocity. This is different from strain rate, which is dependent on a specific  
107 element size [16, 17]. Therefore, slip rate has been used in dynamic studies of Pereira  
108 and Lourenco [15] and Li [16]. Following these studies, the authors also adopted slip  
109 rate in the current study to describe the dynamic bond-slip behaviour. The mechanical  
110 behaviour associated with the four parameters ( $E_f t_f$ ,  $b_f$ ,  $L$  and  $f'_c$ ) in the dynamic  
111 tests was analysed through experimental tests. Finally, for applications in finite element  
112 analysis (FEA), constitutive equations of the dynamic bond-slip behaviour were  
113 proposed. The test results and the constitutive equations derived in this study could be  
114 utilised in FEA to replicate CFRP-concrete interface behaviour under impact and blast  
115 loading regimes.

116

## 117 **2. Experimental programme**

118 A total of 75 single-lap shear tests have been conducted to investigate the dynamic  
119 bond-slip behaviour with loading rates ranging from 0.02 mm/s to about 2000 mm/s.  
120 The quasi-static tests with a loading rate of 0.02 mm/s served as the baseline for the  
121 analysis of dynamic tests. Based on different material and geometric features, the  
122 specimens were divided into six groups.

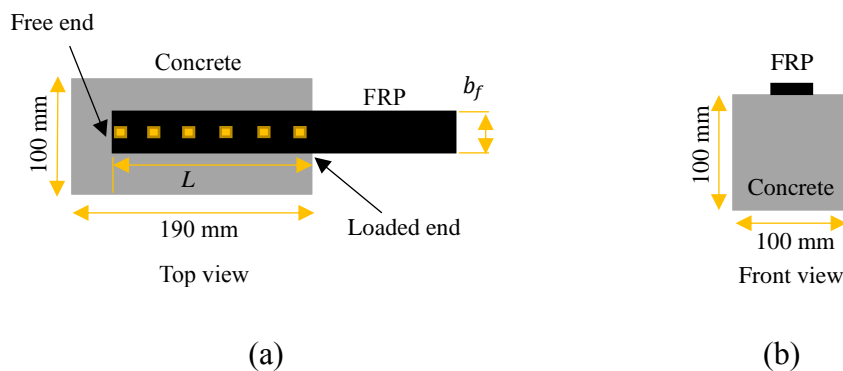
123

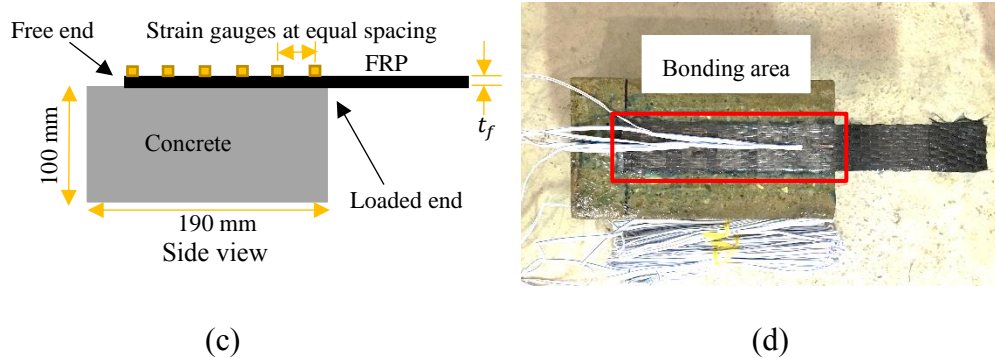
124 In accordance with the loading rate, these tests were classified as quasi-static (0.02  
125 mm/s), low loading-rate (0.8-80 mm/s) and high loading-rate tests (800-2000 mm/s),  
126 respectively. The quasi-static and low loading-rate tests were conducted using an MTS  
127 servo-hydraulic test machine with displacement control, while the high loading-rate  
128 tests were performed with a modified SHPB set-up. In the following sections, the  
129 specimen preparation and the respective test set-up for the low and the high loading  
130 rates will be described.

131

## 132 2.1 Specimen properties

133 As shown in Fig. 2, the specimen consisted of a CFRP sheet bonded to a concrete block.  
134 The specimens were prepared by (a) grinding the concrete surface to reveal the  
135 aggregates, (b) cleaning the exposed substrate using compressed air, and (c) attaching  
136 the CFRP sheet to the concrete block using the epoxy provided by Nitowrap FRC  
137 reinforcement system [18].





140

141

142 Fig. 2. Schematic diagrams of a typical specimen: (a) top view, (b) front view, (c) side  
 143 view and (d) actual specimen

144

145 The concrete block was cast in the same dimensions (100 mm × 100 mm × 190 mm)  
 146 for all 75 specimens. Two concrete grades (C40 and C60) were used to study the  
 147 influence of concrete strength. Table 1 shows the mix proportions of the two concrete  
 148 grades and respective strength of three cylinder samples (Φ150 mm by 300 mm long).  
 149 The 28-day mean cylinder strengths  $f'_c$  were measured as 32.0 MPa and 53.8 MPa for  
 150 the two concrete grades. To suit local practice which adopts cube strength, they were  
 151 designated as C40 and C60 to indicate equivalent cube strength, respectively.

152 Table 1. Mix proportions of concrete (kg/m<sup>3</sup>) and corresponding strengths

Grade	Cement	Sand	Water	Coarse aggregate	Measured strengths (MPa)	Average cylinder strength (MPa)	SD <sup>1</sup> (MPa)
C40	350	720	168	1070	32.5/31.8/31.7	32.0	0.4
C60	535	676	162	930	54.7/53.0/53.6	53.8	0.9

153 <sup>1</sup>means standard deviation (SD)

154

155 The CFRP sheet used in this study was made with a unidirectional fabric of carbon  
 156 fibres and an epoxy which were included in the Nitowrap FRC 300 reinforcement

157 system. The product brochure [18] indicated that the dry fibres and the epoxy had  
158 tensile strength of 3400 MPa and 50 MPa, respectively. The single and double layers of  
159 CFRP were produced with a thickness  $t_f$  of 0.5 mm and 1.0 mm, respectively. After  
160 fabricating a single layer of CFRP sheet, tensile strength  $f_{tf}$  and elastic modulus  $E_f$   
161 were measured as 750 MPa and 82.7 GPa, respectively, using the test method described  
162 in ASTM D3039/D3039M-00 [19]. Since the CFRP stiffness is equal to its elastic  
163 modulus multiplied by its thickness ( $E_f t_f$ ), the stiffness values of single and double  
164 layers were 41.4 and 82.7 GPa·mm, respectively.

165

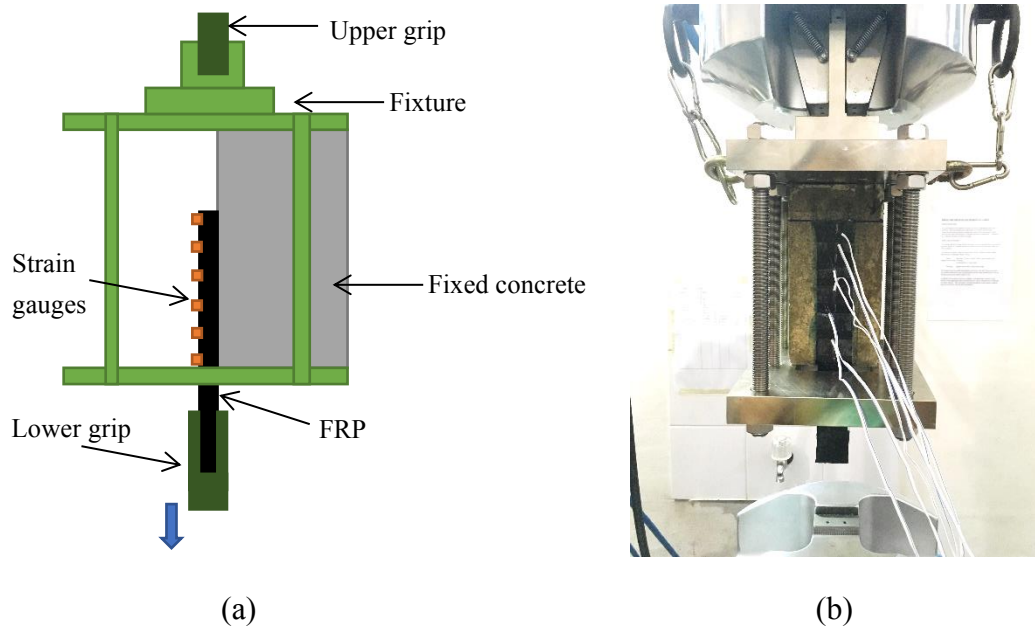
166 To investigate the effect of CFRP parameters on the specimens, CFRP sheets were  
167 varied including the stiffness ( $E_f t_f=41.4$  or  $82.7$  GPa·mm), bond width ( $b_f=26$  or  $33$   
168 mm) and bond length ( $L=75, 100$  or  $150$  mm). For specimens with three different  
169 lengths, four, five and six strain gauges were arranged on the CFRP surface within the  
170 bonded part at equal spacing, respectively. The strain gauge (Type UFLA-5-11-5LT)  
171 produced by TML<sup>®</sup> had a length of 5 mm and aimed to measure strain values of  
172 composite and metal materials. Through varying the concrete and CFRP parameters,  
173 these specimens could be used to investigate the influence of the four parameters ( $E_f t_f$ ,  
174  $b_f$ ,  $L$  and  $f'_c$ ) in the dynamic tests.

175

## 176 **2.2 Quasi-static and low loading-rate tests**

177 Fig. 3 shows the test set-up for the quasi-static and low loading-rate tests (0.02- 80  
178 mm/s). The specimen was placed vertically in an MTS servo-hydraulic test machine

179 and its CFRP sheet was clamped by the lower grip and loaded with displacement control.  
180 The loading rates of the tests were specified using the test machine control system. The  
181 load cell in the actuator was used to record the applied force, and strain gauges on the  
182 CFRP surface were arranged to measure axial strain of the bonded area. A high-  
183 frequency data logger was used to collect the strain measurements. To minimise  
184 eccentric loading, a fixture was manufactured to align the bonded interface of the  
185 specimen with the loading direction, as shown in Fig. 3.



186  
187 (a) (b)  
188 Fig. 3. Test set-up using MTS servo-hydraulic test machine: (a) schematic diagram of  
189 side view and (b) photograph of front view

190  
191 Information on the loading, material and geometric parameters of these tests is given in  
192 Table 2. It includes the loading rate, concrete strength  $f'_c$ , stiffness and thickness of the  
193 CFRP ( $E_f t_f$  and  $t_f$ ), width and length of the CFRP-concrete bonding interface ( $b_f$   
194 and  $L$ ). The nomenclature of the specimens contained information on the loading rate,

195 indicated by M1, M2, M3 or M4 prefix (0.02, 0.8, 8.0 and 80 mm/s), followed by the  
 196 concrete grade as C40 or C60. The final number, ranging from 1 to 5, was used to  
 197 distinguish different sizes of FRP sheets. Three samples (A, B, C) were prepared for  
 198 each testing configuration to evaluate repeatability. For specimens tested under low  
 199 loading rates (M1 and M2), the loads were imposed with a ramp mode which  
 200 incorporated the acceleration range from 0 to the target rate in the entire loading process.  
 201 However, to maintain a stable loading rate in the dynamic regime (M3 and M4), the  
 202 actuator was accelerated to the loading rate first and then the sample was loaded.

203 Table 2. Test items on the servo-hydraulic test machine

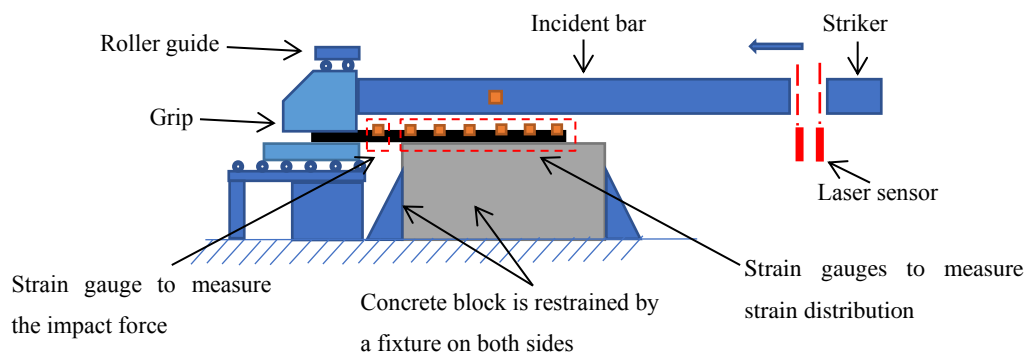
Test	Loading rate (mm/s)	$f'_c$ (MPa)	$E_f t_f$ (GPa-mm)	$t_f$ (mm)	$b_f$ (mm)	$L_f$ (mm)	Number	
C40-1	M1-C40-1	0.02	32.0	41.4	0.5	33	150	A, B, C (3)
	M2-C40-1	0.8	32.0	41.4	0.5	33	150	A, B, C (3)
	M3-C40-1	8.0	32.0	41.4	0.5	33	150	A, B, C (3)
	M4-C40-1	80	32.0	41.4	0.5	33	150	A, B, C (3)
C40-2	M1-C40-2	0.02	32.0	82.7	1.0	33	150	A, B, C (3)
	M4-C40-2	80	32.0	82.7	1.0	33	150	A, B, C (3)
C40-3	M1-C40-3	0.02	32.0	41.4	0.5	26	150	A, B, C (3)
	M4-C40-3	80	32.0	41.4	0.5	26	150	A, B, C (3)
C40-4	M1-C40-4	0.02	32.0	41.4	0.5	33	100	A, B, C (3)
	M4-C40-4	80	32.0	41.4	0.5	33	100	A, B, C (3)
C40-5	M1-C40-5	0.02	32.0	41.4	0.5	33	75	A, B, C (3)
	M4-C40-5	80	32.0	41.4	0.5	33	75	A, B, C (3)
C60-1	M1-C60-1	0.02	53.8	41.4	0.5	33	150	A, B, C (3)
	M3-C60-1	8.0	53.8	41.4	0.5	33	150	A, B, C (3)
	M4-C60-1	80	53.8	41.4	0.5	33	150	A, B, C (3)

204

### 205 2.3 High loading-rate tests

206 As the loading rate of the servo-hydraulic test machine was limited by the capacity of  
 207 its hydraulic oil pump, the set-up could not be used for high loading-rate tests. A

208 modified SHPB set-up could be used for this purpose. A normal SHPB set-up consists  
 209 of a striker bar, an incident bar and a transmission bar [20], all of which are made of  
 210 high-strength steel. The specimen is placed between the incident bar and the  
 211 transmission bar and is loaded by a compressive impulse wave from the incident bar.  
 212  
 213 Since it was not possible to test CFRP-concrete specimens using the normal SHPB  
 214 machine, the set-up had to be modified to conduct high loading-rate shear tests. As  
 215 depicted in Figs. 4(a) and 4(b), the transmission bar was removed and replaced by a  
 216 grip, which was constrained by a roller guide to have horizontal movement only. The  
 217 upper part of the grip was in contact with the incident bar to transfer the impact load so  
 218 that the whole grip would move along the roller guide. Below the incident bar (Fig.  
 219 4(a)), the CFRP sheet was clamped in the grip and was pulled in the horizontal direction  
 220 upon impact. Both the grip and the roller guide were fabricated using DF3 steel, a tool  
 221 steel with a high yield strength of 1800 MPa. During the impact test, the concrete block  
 222 was restrained from movement by a fixture on each side.



223

224

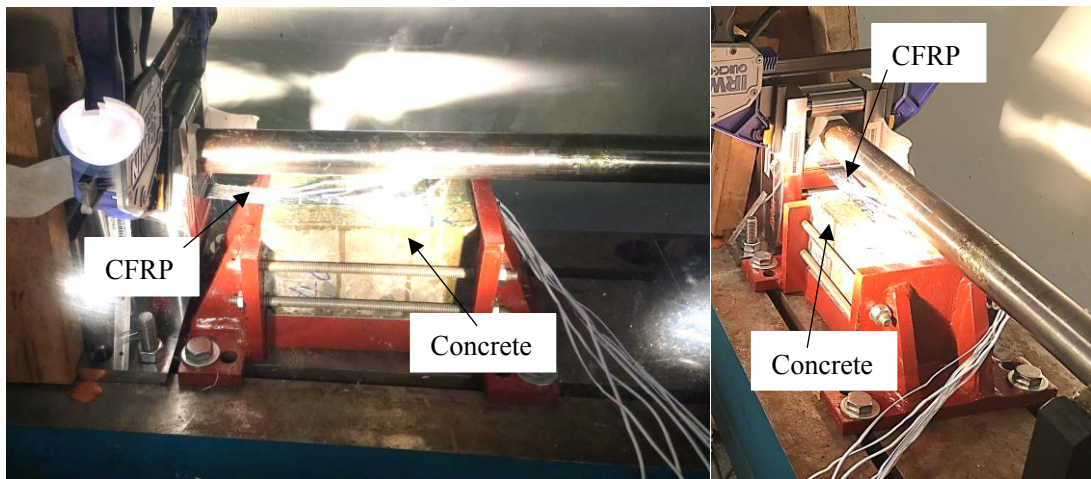
(a) Schematic diagram of test set-up



225

226

(b) Grip and roller guide



227

228

(c) Photograph of the modified SHPB test

229

Fig. 4. Bond-slip test set-up using modified SHPB

230

231 The measurement system is shown in Figs. 4(a) and 4(c). Six equally-spaced strain  
 232 gauges were placed on the bonded region to measure CFRP strain distribution along the  
 233 loading direction. Since no load cell was available for this test set-up, one additional  
 234 strain gauge was placed on the CFRP sheet ahead of the bonding area to measure the  
 235 impact force applied onto the specimen. A high-frequency data logger was used to  
 236 collect strain measurements at a frequency of 1 MHz.

237

238 Table 3 summarises the tests conducted with the modified SHPB set-up. The loading  
239 rate of the tests was controlled by air pressure in the gas gun. Since there was no direct  
240 measurement for loading rate in this set-up, the S1 and S2 designation represent an  
241 applied air pressure of 1.5 bar and 3.5 bar in the gas gun, respectively. The meanings of  
242 the notations in Table 3 are the same as those for the quasi-static and low loading-rate  
243 tests as described for Table 2.

244

245 Prior to the impact tests, two specimens were tested under the air pressure of 4.0 bar  
246 and 1.0 bar to find an appropriate range for the impact load. The test under 4.0 bar  
247 caused visible bending of one roller indicating that the applied load had exceeded the  
248 capacity of the roller guide. On the other hand, the loading produced with a pressure of  
249 1.0 bar was too low to entirely separate CFRP sheet from the concrete surface,  
250 indicating an unsuccessful test. Therefore, to avoid both situations, the specimens were  
251 tested under an air pressure of 1.5 bar or 3.5 bar. Similar to the tests conducted on the  
252 servo-hydraulic machine, three samples (i.e. A, B, C) were prepared for each  
253 configuration.

Table 3. Test items on the modified SHPB

Test	Air pressure (bar)	$f'_c$ (MPa)	$E_f t_f$ (GPa·mm)	$t_f$ (mm)	$b_f$ (mm)	$L_f$ (mm)	Number
C40-1	S1-C40-1	1.5	32.0	41.4	0.5	33	A, B, C (3)
	S2-C40-1	3.5	32.0	41.4	0.5	33	A, B, C (3)
C40-2	S1-C40-2	1.5	32.0	82.7	1.0	33	A, B, C (3)
	S2-C40-2	3.5	32.0	82.7	1.0	33	A, B, C (3)
C40-3	S1-C40-3	1.5	32.0	41.4	0.5	26	A, B, C (3)
C40-4	S1-C40-4	1.5	32.0	41.4	0.5	33	A, B, C (3)
	S2-C40-4	3.5	32.0	41.4	0.5	33	A, B, C (3)
C40-5	S1-C40-5	1.5	32.0	41.4	0.5	33	75 A, B, C (3)
C60-1	S1-C60-1	1.5	53.8	41.4	0.5	33	A, B, C (3)
	S2-C60-1	3.5	53.8	41.4	0.5	33	A, B, C (3)

255

256 **3. Test Results**257 **3.1 Quasi-static behaviour**

258 Quasi-static test results were assessed by comparing with model predictions by other  
259 researchers. Based on finite element simulations and regression analysis of existing  
260 quasi-static tests, Lu et al. [3] derived a bond-slip model to predict peak bond stress  $\tau_{st}$   
261 and interface fracture energy  $G_{fst}$  of FRP-concrete bond interface, as follows.

$$262 \quad \tau_{st} = \alpha_1 \beta_w f_t \quad (1)$$

$$263 \quad G_{fst} = 0.308 \beta_w^2 \sqrt{f_t} \quad (2)$$

264 where  $\alpha_1$  is a coefficient determined from regression and is given by 1.5,  $\beta_w$  is the  
265 bond width coefficient and  $f_t$  is the concrete tensile strength.

266

267 With interface fracture energy, the ultimate load  $P_u$  of single-lap shear test can be  
268 predicted by [3, 12, 21, 22]:

269 
$$P_u = \beta_L b_f \sqrt{2E_f t_f G_{fst}} \quad (3)$$

270 where  $\beta_L$  is the bond length coefficient,  $b_f$  is the bond width of CFRP sheet and  $E_f t_f$   
 271 is the CFRP stiffness.

272

273 The bond width coefficient  $\beta_w$  is to account for different widths of the FRP ( $b_f$ ) and  
 274 the concrete substrate ( $b_c$ ) [2, 3].

275 
$$\beta_w = \sqrt{\frac{2-b_f/b_c}{1+b_f/b_c}} \quad (4)$$

276

277 The bond length coefficient is a piecewise function related to effective bond length  $L_e$ ,  
 278 as shown in Eq. (5) [2, 3]. When the bond length  $L$  is smaller than  $L_e$ , an increase of  
 279  $L$  would change  $\beta_L$ . However, any increase in bond length over  $L_e$  would not  
 280 improve ultimate load.

281 
$$\beta_L = \begin{cases} 1 & \text{if } L \geq L_e \\ \sin \frac{\pi L}{2L_e} & \text{if } L < L_e \end{cases} \quad (5)$$

282 where effective bond length  $L_e$  is defined as  $L_e = \sqrt{\frac{E_f t_f}{\sqrt{f'_c}}}$ .

283

284 To assess the accuracy of model predictions, the authors' results of the quasi-static tests  
 285 were compared with the model predictions by Lu et al. [3]. The results are shown in  
 286 Table 4 and Fig. 5. The coefficients of variation (CoV) of ultimate load  $P_u$  and peak  
 287 bond stress  $\tau_{st}$  were in the range of 1.0% to 16.2%. This showed that the repeated tests  
 288 produced consistent results. The ratio between the test results and the predicted values  
 289 were reasonable, varying between 0.81 and 1.05, indicating that the model by Lu et al.

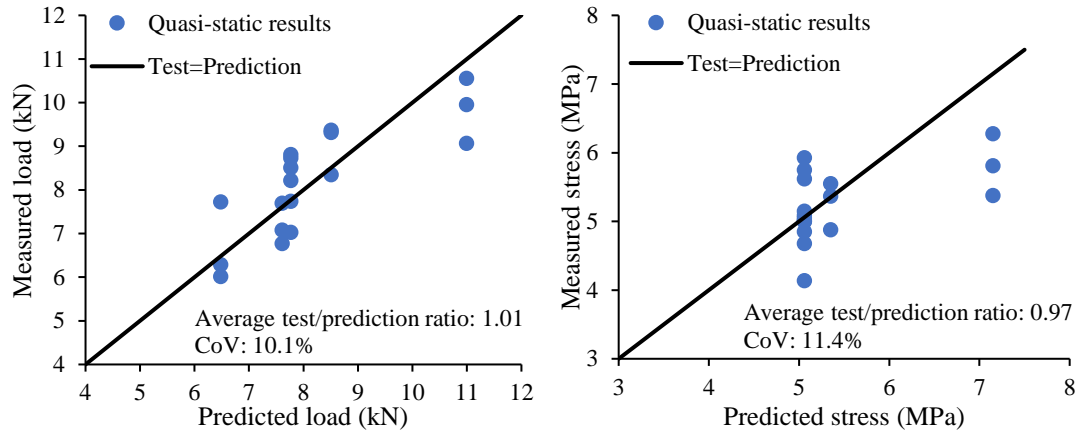
290 [3] could properly predict these quasi-static tests. The overestimation of peak bond  
 291 stress in M1-C60-1 specimens showed that Lu's model might overstate this property  
 292 for samples with high strength concrete. As Lu's model [3] has been widely used in  
 293 analyses of FRP strengthened concrete structures, the predictions of peak bond stress  
 294 and interface fracture energy were used as the baseline for dynamic increase factor (DIF)  
 295 values of dynamic test results.

296 Table 4. Quasi-static test results and comparison with predictions from Lu's model[3]

Item	$P_u$ in tests (kN)	Average (kN)/ CoV	$P_u$ by model (MPa) [3]	Ratio of test/ model	$\tau_{st}$ in tests (MPa)	Average (MPa)/ CoV	$\tau_{st}$ by model (MPa) [3]	Ratio of test/ model
M1-C40-1A	8.22				5.05			
M1-C40-1B	8.51	8.16/	7.77	1.05	5.15	5.10/	5.06	1.01
M1-C40-1C	7.74	4.8%			5.09	1.0%		
M1-C40-2A	9.96				5.02			
M1-C40-2B	9.07	9.86/	10.99	0.90	4.14	4.97/	5.06	0.98
M1-C40-2C	10.56	7.6%			5.75	16.2%		
M1-C40-3A	6.02				4.88			
M1-C40-3B	7.73	6.68/	6.48	1.03	5.37	5.27	5.35	0.99
M1-C40-3C	6.29	13.8%			5.55	6.6%		
M1-C40-4A	8.73				4.68			
M1-C40-4B	8.81	8.19/	7.77	1.05	5.62	5.10/	5.06	1.01
M1-C40-4C	7.03	12.3%			5.00	9.4%		
M1-C40-5A	7.08				5.00			
M1-C40-5B	7.70	7.18/	7.61	0.94	4.85	5.26/	5.06	1.04
M1-C40-5C	6.77	6.5%			5.93	11.1%		
M1-C60-1A	8.35				6.28			
M1-C60-1B	9.32	9.02/	8.51	1.04	5.81	5.82/	7.15	0.81
M1-C60-1C	9.37	6.4%			5.38	7.7%		

297 Note: all specimens in Table 4 were failed by debonding in concrete.

298



299

300

(a)

(b)

301 Fig. 5 Comparison of quasi-static test results with predictions via Lu's model [3] for

302 (a) ultimate load and (b) peak bond stress

303

### 304 3.2 Test results and failure modes

305 Fig. 6 presents typical layers in CFRP strengthened RC structures and locations of

306 possible debonding failure as reported in literature [23]. For classification purpose,

307 failure modes of the specimens in this study were recorded as debonding in concrete

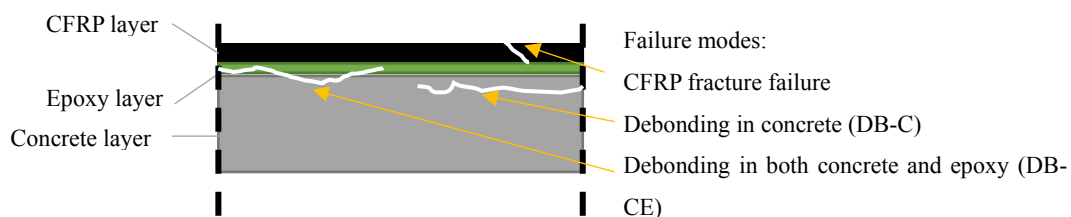
308 (DB-C), debonding in concrete and epoxy (DB-CE), debonding and CFRP failure at the

309 edge (DB-CFE), CFRP failure at middle (CFM) and CFRP not debonding but failure at

310 the edge (NDB-CF), as shown in Fig. 7. The debonded CFRP sheet was placed next to

311 the concrete substrate to show the failure mode and its extent. The failure mode of each

312 test is indicated in Table 5.

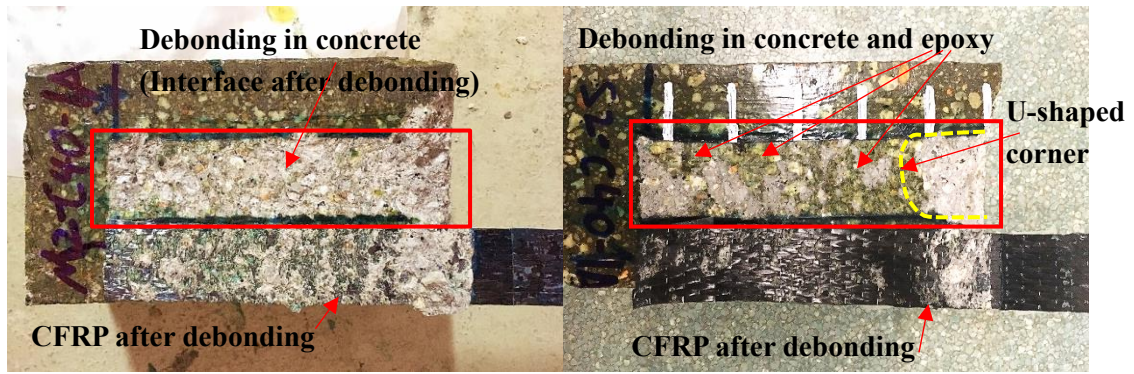


313

314

Fig. 6. Bond failure at different layers

315

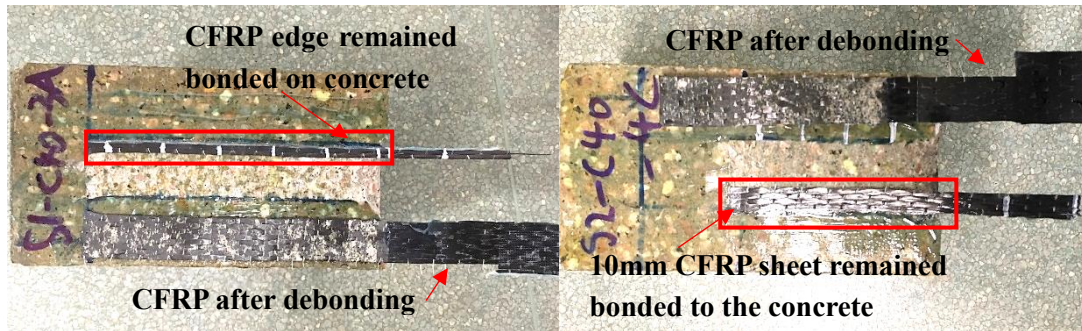


316

317

(a) Debonding in concrete (DB-C)

(b) Debonding in concrete and epoxy (DB-CE)

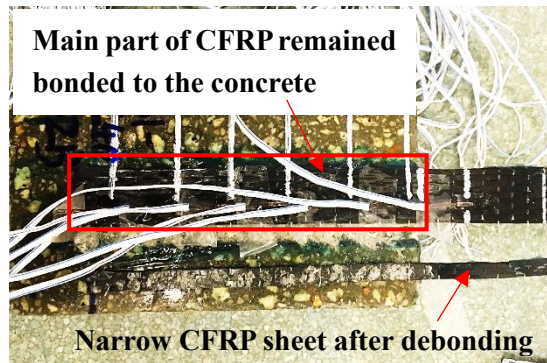


318

319

(c) Debonding and CFRP failure at edge (DB-CFE)

(d) CFRP failure at middle (CFM)



320

321

(e) Not debonding and CFRP failure at edge (NDB-CF)

322

Fig. 7. Different failure modes of testing specimens

323

324 In these tests, sixty out of the seventy-five specimens failed by debonding in the

325 concrete layer (DB-C), which left some mortar and sands attached to the CFRP sheet,

326 as shown in Fig. 7(a). The thickness of this separated concrete layer below the bond

327 interface varied from about 0.5 mm to 4 mm. This result was commonly observed in

328 the published literature on CFRP-concrete debonding tests [1, 3]. Since tensile strength  
329 and shear strength of concrete are always weaker than epoxy strength of 50 MPa, failure  
330 process started from cracking of concrete at the loaded end of the specimen (Fig. 2(a)).  
331 With an increase of applied load, more cracks appeared in the concrete layer below the  
332 bond interface and failure propagated to the free end of the bonded area.

333

334 Ten specimens under dynamic load showed a second failure mode in which cracks  
335 formed in both the concrete and the epoxy (DB-CE), as shown in Fig. 7(b). Similar to  
336 the first failure mode, a lump of concrete spalled off from the loaded end, which meant  
337 that cracks also started from the concrete layer. After separation from the concrete  
338 substrate, less concrete was attached to the CFRP sheet and some epoxy lumps were  
339 left on the concrete block. This failure mode could be attributed to dynamic load  
340 causing greater stress concentration at different locations between the two materials.  
341 Specifically, after concrete spalling at the loaded end in Fig. 6(b), the U-shaped corner  
342 experienced stress concentration in the epoxy layer and resulted in debonding of the  
343 epoxy layer around the corner.

344

345 In the dynamic tests using the modified SHPB, four specimens failed due to CFRP  
346 failure along the fibre direction, as shown in Figs. 7(c) and 7(d). Majority of the CFRP  
347 sheet of specimen S1-C40-3A debonded from the concrete. However, it split  
348 longitudinally and a 4 mm wide strip at the left edge remained affixed on the concrete  
349 surface, as shown in Fig. 7(c). Specimen S2-C40-4C showed more severe longitudinal

350 damage, with a 10 mm wide of CFRP remaining on the concrete in Fig. 7(d). Specimens  
351 S2-C60-1B and S2-C60-1C also failed in the same way. To investigate the reason for  
352 the CFRP fracture, tensile strength of the composite sheet was obtained as 750 MPa.  
353 The sectional dimensions of the sheets used for S1-C40-3 and S2-C40-4 were 26 mm  
354  $\times$  0.5 mm and 33 mm  $\times$  0.5 mm, respectively. Multiplying these areas by its tensile  
355 strength, the estimated load capacities were 9.75 kN and 12.38 kN, respectively. The  
356 measured ultimate loads for the three tests of S1-C40-3A, B and C were between 9.30  
357 kN and 10.04 kN, close to the estimated value of 9.75 kN. In the same way, the ultimate  
358 loads measured in the tests of S2-C40-4 specimens were between 12.10 kN and 14.42  
359 kN, compared to the capacity of 12.38 kN. Therefore, this simple calculation shows that  
360 CFRP fracture in these specimens was caused by ultimate loads exceeding the  
361 respective CFRP fracture capacity. Since strain gauges were attached on the CFRP  
362 surface in these shear tests, the CFRP fracture behaviour made tests of S2-C40-4C, S2-  
363 C60-1B and S2-C60-1C have no valid data for the interface debonding study.

364

365 As shown in Fig. 7(e), the specimen S1-C40-2B failed with only a narrow part of the  
366 CFRP debonding, while a large portion of the sheet remained intact. In this case, unlike  
367 the other CFRP fracture scenarios, the load was significantly lower than the composite  
368 capacity. Therefore, this result could have been due to poor workmanship of the CFRP  
369 sheet itself. Though this particular sample failed to provide useful data, the repeated  
370 tests S1-C40-2A and S1-C40-2C gave reliable results and were used in the statistical  
371 analysis.

372

373 All the test results of seventy-five specimens are presented in Table 5. Six types of  
374 specimens with different material and geometric properties were tested for parametric  
375 investigation. Specimens C40-1 were a control group with a single-layer CFRP sheet.  
376 A double-layer CFRP sheet and a narrower CFRP sheet were used in specimens C40-2  
377 and C40-3 to investigate the effect of CFRP stiffness and width, respectively.  
378 Specimens C40-4 and C40-5 were used to study the effect of bond length under  
379 dynamic loading. To study dynamic debonding response with different concrete  
380 strengths, higher concrete strength was adopted for C60-1 specimens. The DIF was  
381 calculated as the ratio of each dynamic test result divided by the corresponding quasi-  
382 static predictions by Lu's model [3].

383

Table 5. Summary of all test results

Specimens		Slip rate (mm/s)	$d_u$ (mm)	$P_u$ (kN)	$\tau_{max}$ (MPa)	DIF of $\tau_{max}$	Initial stiffness (MPa/mm)	$G_f$ (N/mm)	DIF of $G_f$	Failure mode
C40-1	M1-C40-1A	3.90e-3	0.78	8.22	5.05	1.00	65.5	0.86	1.31	DB-C
	M1-C40-1B	4.50e-3	0.74	8.51	5.15	1.02	84.9	0.76	1.13	DB-C
	M1-C40-1C	4.70e-3	0.70	7.74	5.09	1.01	90.8	0.63	0.94	DB-C
	M2-C40-1A	2.37e-1	0.83	9.84	5.83	1.15	92.3	1.04	1.55	DB-C
	M2-C40-1B	2.28e-1	0.75	8.17	4.90	0.97	89.9	0.81	1.21	DB-C
	M2-C40-1C	2.26e-1	0.71	8.07	5.88	1.16	96.1	0.81	1.21	DB-C
	M3-C40-1A	2.46	0.83	9.38	5.57	1.10	85.5	1.15	1.72	DB-CE
	M3-C40-1B	2.16	0.71	8.92	5.75	1.14	86.0	0.88	1.31	DB-C
	M3-C40-1C	2.38	0.79	8.70	6.09	1.20	97.3	0.90	1.34	DB-C
	M4-C40-1A	31.83	0.88	10.27	5.93	1.17	84.5	1.21	1.81	DB-C
	M4-C40-1B	25.12	0.85	9.34	6.04	1.19	88.6	0.82	1.22	DB-C
	M4-C40-1C	26.85	0.84	10.09	6.46	1.28	92.0	1.12	1.67	DB-C
	S1-C40-1A	1541	0.94	12.45	6.88	1.36	58.3	1.47	2.19	DB-C
	S1-C40-1B	1786	0.88	11.74	9.85	1.94	98.0	1.79	2.67	DB-CE
	S1-C40-1C	1127	0.83	11.39	7.51	1.48	84.7	1.14	1.70	DB-C
	S2-C40-1A	1509	1.07	14.71	8.71	1.72	96.3	1.98	2.96	DB-CE
S2-C40-1B	2150	1.16	11.79	8.77	1.73	95.8	1.81	2.70	DB-CE	
S2-C40-1C	1927	1.22	14.12	9.81	1.94	89.4	2.05	3.06	DB-CE	
C40-2	M1-C40-2A	4.60e-3	0.48	9.96	5.02	0.99	114.6	0.64	0.96	DB-C
	M1-C40-2B	4.10e-3	0.44	9.07	4.14	0.82	116.2	0.47	0.70	DB-C
	M1-C40-2C	3.50e-3	0.41	10.56	5.75	1.14	125.0	0.81	1.21	DB-C
	M4-C40-2A	22.08	0.54	14.44	6.83	1.35	129.0	0.96	1.43	DB-C
	M4-C40-2B	25.06	0.61	14.00	7.30	1.44	123.0	1.12	1.67	DB-C
	M4-C40-2C	24.49	0.72	14.11	8.88	1.75	138.3	1.60	2.39	DB-C
	S1-C40-2A	807	0.76	19.46	9.76	1.93	169.1	1.98	2.96	DB-C
	S1-C40-2B	—	—	—	—	—	—	—	—	NDB-CF
	S1-C40-2C	849	0.76	21.59	10.07	1.99	153.9	1.90	2.84	DB-C
	S2-C40-2A	1371	0.74	18.29	9.25	1.83	172.1	1.90	2.84	DB-C
	S2-C40-2B	1176	0.79	19.32	11.99	2.37	172.2	1.86	2.78	DB-C
S2-C40-2C	1676	0.88	21.39	9.87	1.95	166.9	2.21	3.30	DB-C	
C40-3	M1-C40-3A	4.10e-3	0.61	6.02	4.88	0.91	96.3	0.59	0.79	DB-C
	M1-C40-3B	4.10e-3	0.87	7.73	5.37	1.00	86.8	0.78	1.04	DB-C
	M1-C40-3C	4.70e-3	0.74	6.29	5.55	1.04	94.0	0.65	0.87	DB-C
	M4-C40-3A	43.30	1.10	9.47	7.21	1.35	91.1	1.55	2.07	DB-C
	M4-C40-3B	41.47	0.91	8.68	6.89	1.29	87.8	1.08	1.44	DB-C
	M4-C40-3C	37.09	0.96	9.94	6.97	1.30	88.5	1.28	1.71	DB-C
	S1-C40-3A	2077	1.05	10.04	8.16	1.52	102.7	1.63	2.17	DB-CFE

(Continued on next page)

Table 5. (continued)

Specimens		Slip rate (mm/s)	$d_u$ (mm)	$P_u$ (kN)	$\tau_{max}$ (MPa)	DIF of $\tau_{max}$	Initial stiffness (MPa/mm)	$G_f$ (N/mm)	DIF of $G_f$	Failure mode
C40-3	S1-C40-3B	2017	1.00	9.30	7.84	1.46	97.7	1.12	1.49	DB-CE
	S1-C40-3C	1873	1.10	9.46	7.95	1.48	97.1	1.49	1.99	DB-C
C40-4	M1-C40-4A	4.60e-3	0.39	8.73	4.68	0.92	122.5	0.50	0.75	DB-C
	M1-C40-4B	4.20e-3	0.53	8.81	5.62	1.11	119.5	0.68	1.01	DB-C
	M1-C40-4C	4.30e-3	0.37	7.03	5.00	0.99	107.2	0.50	0.75	DB-C
	M4-C40-4A	24.31	0.63	9.89	8.30	1.64	143.7	1.25	1.87	DB-CE
	M4-C40-4B	21.66	0.50	8.76	6.69	1.32	125.0	0.90	1.34	DB-C
	M4-C40-4C	23.82	0.53	9.10	7.31	1.44	140.7	0.94	1.40	DB-C
	S1-C40-4A	845	0.71	11.50	9.83	1.94	144.0	1.56	2.32	DB-C
	S1-C40-4B	841	0.74	13.01	7.83	1.55	134.2	1.59	2.37	DB-CE
	S1-C40-4C	743	0.70	12.38	9.02	1.78	145.3	1.47	2.19	DB-C
	S2-C40-4A	1521	0.90	14.42	8.91	1.76	96.4	1.73	2.58	DB-C
	S2-C40-4B	1858	0.80	12.10	10.07	1.99	137.1	1.61	2.40	DB-C
	S2-C40-4C	—	—	13.60	—	—	—	—	—	CFM
C40-5	M1-C40-5A	4.00e-3	0.35	7.08	5.00	0.99	105.4	0.53	0.79	DB-C
	M1-C40-5B	3.70e-3	0.31	7.70	4.85	0.96	112.1	0.52	0.78	DB-C
	M1-C40-5C	3.60e-3	0.30	6.77	5.93	1.17	138.8	0.53	0.79	DB-C
	M4-C40-5A	15.33	0.39	9.46	6.94	1.37	116.2	0.90	1.34	DB-C
	M4-C40-5B	16.24	0.36	8.40	6.77	1.34	148.9	0.77	1.15	DB-C
	M4-C40-5C	16.85	0.39	7.41	8.23	1.63	154.5	1.13	1.69	DB-C
	S1-C40-5A	595	0.52	11.50	7.99	1.58	103.3	1.30	1.94	DB-CE
	S1-C40-5B	655	0.54	12.73	8.35	1.65	150.3	1.36	2.03	DB-C
	S1-C40-5C	818	0.52	11.00	9.93	1.96	159.8	1.27	1.90	DB-C
C60-1	M1-C60-1A	6.10e-3	0.88	8.35	6.28	0.88	96.2	0.93	1.17	DB-C
	M1-C60-1B	5.10e-3	0.83	9.32	5.81	0.81	91.5	1.00	1.26	DB-C
	M1-C60-1C	4.60e-3	0.76	9.37	5.38	0.75	96.3	0.89	1.12	DB-C
	M3-C60-1A	2.60	0.91	10.58	6.27	0.88	83.2	1.26	1.58	DB-C
	M3-C60-1B	2.44	0.77	9.84	5.93	0.83	91.9	0.93	1.17	DB-C
	M3-C60-1C	2.36	0.79	8.82	6.26	0.88	96.1	0.92	1.15	DB-C
	M4-C60-1A	31.43	0.90	9.83	8.02	1.12	96.9	1.32	1.66	DB-C
	M4-C60-1B	29.17	0.91	9.79	7.34	1.03	98.9	1.11	1.39	DB-C
	M4-C60-1C	29.32	0.89	10.25	7.61	1.06	93.9	1.23	1.54	DB-C
	S1-C60-1A	1206	1.16	12.92	8.56	1.20	101.7	1.75	2.20	DB-C
	S1-C60-1B	1211	1.10	12.87	8.23	1.15	98.5	1.53	1.92	DB-CE
	S1-C60-1C	1262	1.15	12.38	9.22	1.29	99.7	1.76	2.21	DB-C
	S2-C60-1A	2031	1.11	13.85	8.21	1.15	99.2	1.64	2.06	DB-C
	S2-C60-1B	—	—	14.23	—	—	—	—	—	CFM
S2-C60-1C	—	—	13.19	—	—	—	—	—	CFM	

386 Note: DB-C, debonding in concrete; DB-CE, debonding in concrete and epoxy; NDB-CF, not  
387 debonding and CFRP failure at edge; DB-CFE, debonding and CFRP failure at edge; CFM,  
388 CFRP failure at middle.

389

### 390 **3.3 Rate effect on load-displacement behaviour**

391 The general failure process of the specimens could be studied using the load-  
392 displacement curves. The load values were recorded by the built-in load cell in the test  
393 machine and the high-frequency data logger. However, the displacements recorded by  
394 the test machine always included relative slip between the grip and the CFRP sheet, and  
395 deformations of the supporting fixture [1]. To obtain more accurate load-displacement  
396 curves, relative slip measurements at the loaded end of the bonded area were used to  
397 represent the displacement values. Dai et al. [4] proposed Eq. (6) to calculate the  
398 relative slip. Concrete was assumed to be rigid and has no movement. The slip at an  
399 arbitrary position  $i$  along the CFRP bonding length was calculated by integrating the  
400 CFRP strains starting from the free end, where strain was assumed to be 0, up to location  
401  $i$ .

$$402 \quad s_i = \frac{\Delta x}{2} (\varepsilon_0 + 2 \sum_{j=1}^{i-1} \varepsilon_j + \varepsilon_i) \quad (6)$$

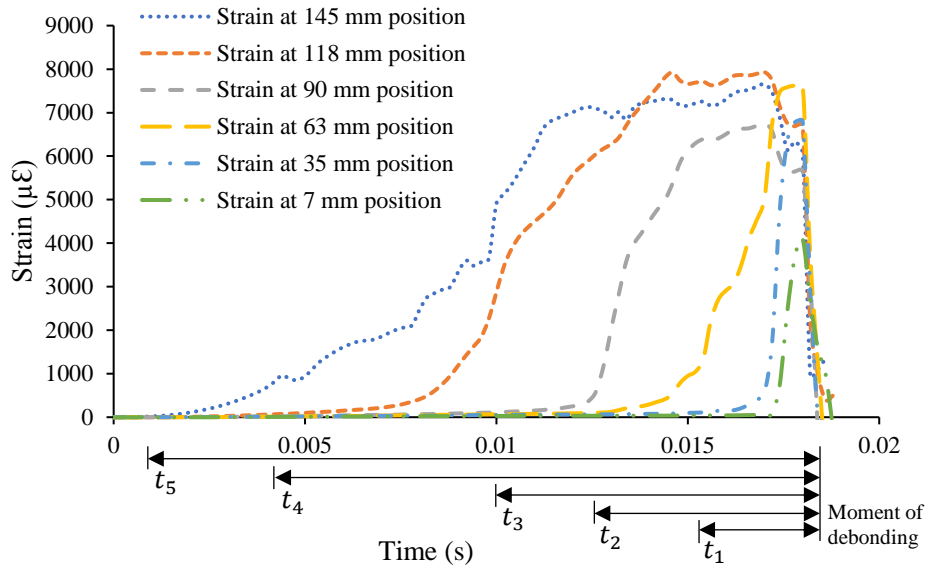
403 where  $s_i$  is the slip at position  $i$ ,  $\Delta x$  is the distance between the strain gauges,  $\varepsilon_0$  is  
404 the strain measured by the strain gauge near the free end (position 0),  $\varepsilon_j$  is the strain  
405 measured between positions 0 and  $i$ , and  $\varepsilon_i$  is the strain value at position  $i$ . Thus, the  
406 slip at the loaded end can be calculated by integrating the strain along the whole bonded  
407 length of CFRP. This method was also adopted in the study of Yuan et al. [21].

408

409 Along the CFRP bond length of 150 mm, the loaded end was defined at the position of  
410 150 mm and the free end was defined to be at 0 mm. Variables  $t_1$  to  $t_5$  in Fig. 8(a)  
411 denote the time required for each bonding point to undergo debonding process. In  
412 accordance with Eq. (6), strain-time curves of 7 mm and 35 mm positions in Fig. 8(a)  
413 were numerically integrated to produce the slip-time curve at 35 mm position in Fig.  
414 8(b). Similarly, the slip -time curve at 63mm positions was derived from integration of  
415 strain -time curves at 7 mm, 35 mm and 63 mm positions, and so on. Parameters  $s_1$  to  
416  $s_5$  in Fig. 8(b) are the respective slip values of each point at the instant of debonding.  
417 It is observed that the gradients of the slip-time curves in Fig. 8(b) were not stable. As  
418 the slip values were the greatest at the loaded end and the smallest near the free end, it  
419 was useful to obtain an average slip rate value to represent the dynamic properties of  
420 each test. The authors decided to use slip-time average equation to obtain an average  
421 slip rate from these slip-time curves for each specimen. The equation to generate the  
422 constant slip rate is given by:

423 
$$\dot{s} = \frac{\sum_{i=1}^n \frac{s_i}{t_i}}{n} \quad (7)$$

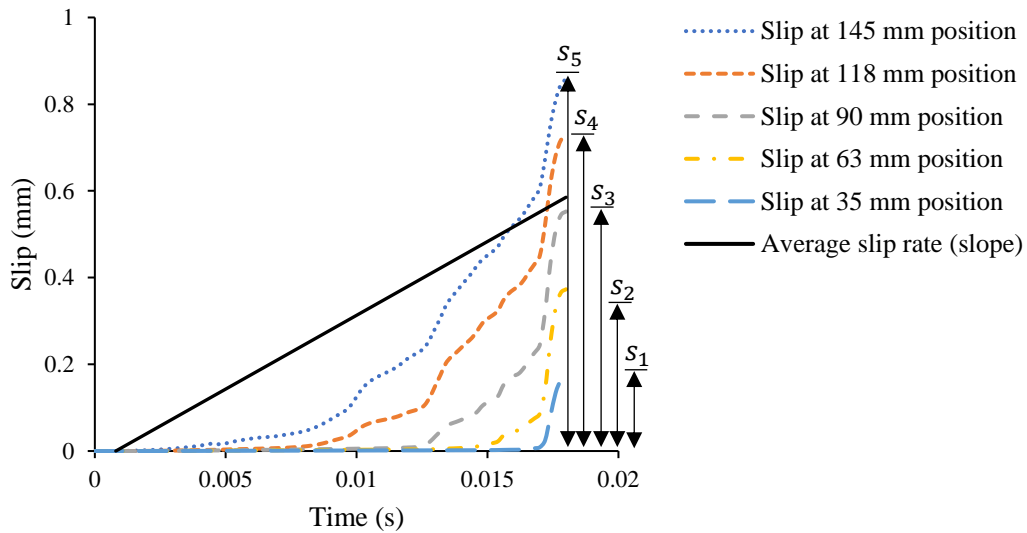
424 where  $n$  is the total number of slip-time curves for a tested specimen. Fig. 8(b) shows  
425 an example of this calculation including the slip-time history of each strain gauge  
426 position and the constant slip rate. The calculated average slip rates are given in Table  
427 5 and are used in subsequent data analyses.



428

429

(a)



430

431

(b)

432 Fig. 8. (a) Strain-time history and (b) slip-time history at each position and average

433 slip rate (M4-C40-1A, average slip rate of 31.83 mm/s)

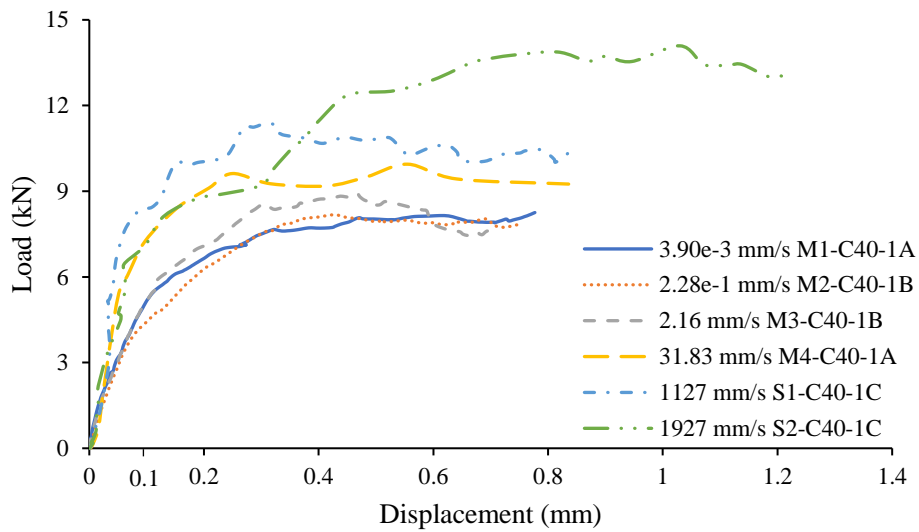
434

435 Fig. 9 presents the load-displacement curves of specimens in the C40-1 group. To

436 highlight the slip-rate effects, curves obtained from the quasi-static tests up to the

437 impact tests were included. The slip rates of these tests were between  $3.90 \times 10^{-3}$  mm/s and

438 1927 mm/s.



439

440 Fig. 9. Load-displacement curves of C40-1 specimens for different slip rates

441

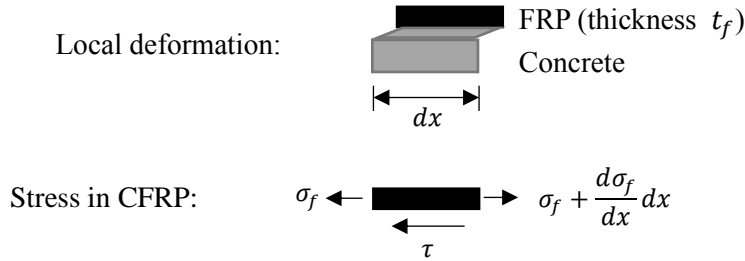
442 In the quasi-static test (M1-C40-1A), the load-displacement curve was close to linear  
443 at initial displacements. After the displacement reached 0.1 mm, the gradient gradually  
444 decreased to zero due to softening caused by local cracks along the bond length. The  
445 specimen had reached its ultimate strength at this stage. This value was maintained and  
446 bond failure propagated towards the free end until the CFRP sheet was totally separated  
447 from the concrete substrate. Specimens tested under higher slip rates generally showed  
448 a similar behaviour but attained higher ultimate loads and larger ultimate displacements.  
449 These phenomena indicated that both the load-carrying capacity and the ultimate  
450 displacement of the bond are sensitive to slip rate effect.

451

### 452 3.4 Rate effect on bond stress-slip behaviour

453 Following the analysis of the load-displacement curves, the differences in bond strength

454 between static and dynamic tests were evaluated. Existing studies proposed a method  
 455 to calculate bond stress  $\tau$  for these tests [3, 4, 12, 13], as shown in Fig. 10. The relevant  
 456 equations are reproduced in Eq. (8) and Eq. (9) [3, 4].



457

458 Fig. 10. Static equilibrium sketch for bond stress  $\tau$

459

460 From Fig. 10, the stress equilibrium equation can be written as:

461 
$$\sigma_f t_f + \tau dx = \left( \sigma_f + \frac{d\sigma_f}{dx} dx \right) t_f \quad (8)$$

462 This equation can be simplified to  $\tau = \frac{d\sigma_f}{dx} t_f$ . Substituting  $\sigma_f = E_f \varepsilon_f$  into Eq. (8),  
 463 shear bond stress  $\tau$  can be calculated as:

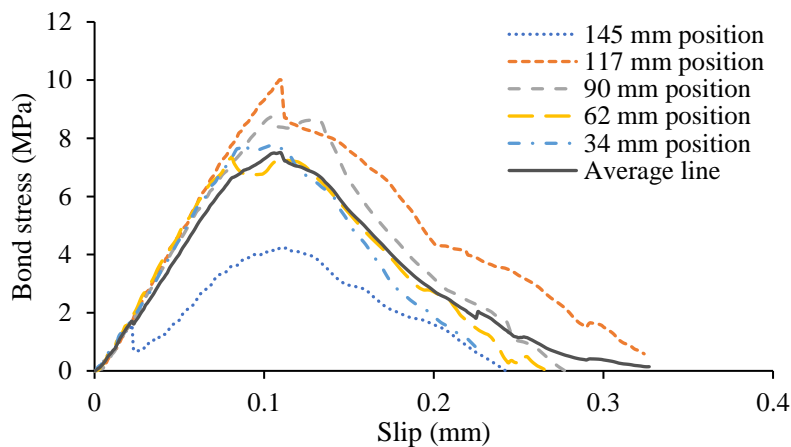
464 
$$\tau = \frac{E_f d\varepsilon_f}{dx} t_f \quad (9)$$

465 where  $\sigma_f$ ,  $t_f$  and  $E_f$  are the axial stress, the thickness and the Young's modulus  
 466 along the loading direction of the CFRP sheet, respectively. To generate bond stress  $\tau$   
 467 at an arbitrary position  $i$ , the difference in axial strain  $d\varepsilon_f$  is obtained using the  
 468 difference in values of two strain gauges adjacent to position  $i$ . The length  $dx$  denotes  
 469 the physical distance between two strain gauges. Since the first strain gauge at the free  
 470 end was the starting point and had zero strain gradient ( $d\varepsilon_f$ ), there were five computing  
 471 points for the six strain gauges on the CFRP (Fig. 2(a)). Following this method, as an  
 472 example, the five bond stress-slip curves of specimen S1-C40-1C are calculated and

473 shown in Fig. 11.

474

475 As the aggregates and mortar were not uniformly distributed in concrete along the bond  
476 length, the bond-slip behaviour of S1-C40-1C at the five points shown in Fig. 11  
477 displayed some differences. The local interfacial bond behaviour is governed by the  
478 average interfacial bond strength and fracture energy [4, 12, 24, 25]. To obtain a  
479 characteristic curve representing an average response along the bonding length, the  
480 curves at all five points were used to generate an average bond-slip curve for each  
481 specimen. The average line is shown as the solid line in Fig.11.



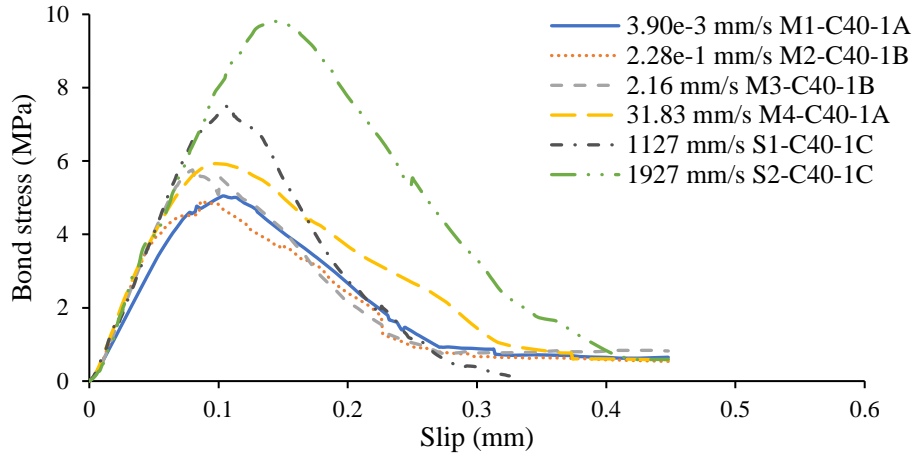
482

483 Fig. 11. Bond stress-slip curves at each position of S1-C40-1C

484

485 Fig. 12 shows the slip-rate effect on bond stress-slip curves of the same six specimens  
486 in Fig. 9, ranging from quasi-static to impact loading regimes. The general shape of  
487 these curves was similar, with a linear ascending range and a gradual softening range.  
488 The results showed the dynamic enhancing effect, with higher peak bond stresses and  
489 larger areas under the graph for specimens tested at higher slip rates. However, except  
490 for the one tested at the lowest rate (M1-C40-1A), the initial slopes of all the curves

491 were similar. This indicated that the initial stiffness values of these bond-slip curves  
 492 were insensitive to slip rate.



493

494 Fig. 12. Bond stress-slip curves of C40-1 specimens under different slip rates

495

496 The initial stiffness value  $E_b$  of the bond is determined from the equation below [26]:

497 
$$E_b = \frac{\Delta\tau}{\Delta s} \quad (10)$$

498 where  $\Delta s$  is the selected slip range in the initial part of the curve in mm and  $\Delta\tau$  is the

499 corresponding increase of bond stress in MPa. In this study,  $\Delta s$  was chosen to be

500 between 0.01 mm and 0.04 mm. To shed light on the slip-rate effect on initial stiffness

501 with material and geometric parameters, Fig. 13 shows the results for specimens in

502 groups C40-1, C40-2, C40-3 and C60-1. Specimens C40-1 were a control group with

503 CFRP stiffness of 41.4 GPa·mm and bond width of 33 mm. Specimens C40-2 had a

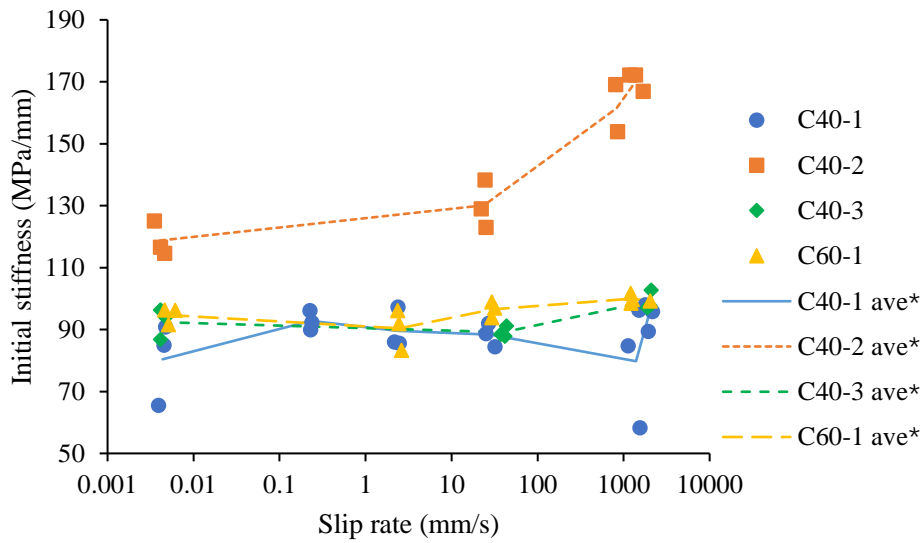
504 higher CFRP stiffness at 82.7 GPa·mm and specimens C40-3 reduced CFRP bond width

505 at 26 mm. Compared with C40-1 specimens, C60-1 specimens adopted higher concrete

506 strength. As the bond lengths of C40-4 and C40-5 specimens were too short to generate

507 complete bond-slip curves, these two groups were excluded from the study of local

508 interface property.



509

510 Fig. 13. Dynamic response of the initial stiffnesses of different specimens (ave\*

511 means an average of 3 tests)

512

513 Among the specimens in groups C40-1, C40-3 and C60-1, there was no clear dynamic

514 enhancing effect, and most of them had similar initial modulus magnitude in the range

515 of 83.2-102.7 MPa/mm. However, the C40-2 specimens, which had a higher CFRP

516 stiffness, showed a higher average quasi-static initial stiffness of 118.8 MPa/mm. The

517 value increased significantly beyond a slip rate of 23.87 mm/s and reached 170.4

518 MPa/mm at the highest rate. The significant rate-dependent response of C40-2

519 specimens might be due to that CFRP sheets in these specimens have the highest

520 stiffness and the dynamic response of the bond is more dependent on the concrete

521 material. Concrete is much more sensitive to the rate effect than CFRP [27, 28].

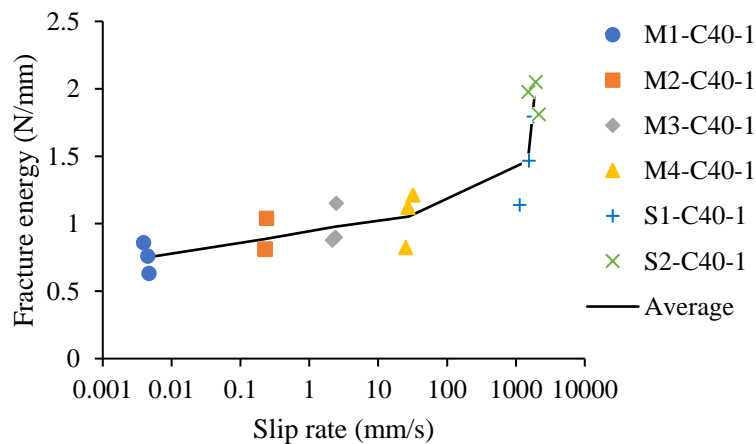
522 Therefore, the data showed that higher composite stiffness ( $E_f t_f$ ) could have rendered

523 the initial stiffness higher and more sensitive to slip rate.

524

### 525 3.5 Rate effect on fracture energy

526 Apart from load-displacement curves and bond stress-slip curves, fracture energy is an  
527 essential property of the interfacial bond. It is defined as the area under bond stress-slip  
528 curves [3]. Fig. 14 shows the fracture energy of specimens C40-1 to assess the dynamic  
529 effect on this property. The results show a nonlinear dynamic enhancement with the  
530 increase of slip rate. The initial range, between a slip rate of 0.004 mm/s and 50 mm/s,  
531 is approximately linear. After this, the gradient increases and the fracture energy  
532 increases significantly at a slip rate of about 2000 mm/s, indicating that the interface  
533 bond is more sensitive to high slip rates. As the dynamic behaviour of the interface bond  
534 largely depends on concrete dynamic response [12], this phenomenon might be  
535 attributed to the fact that, at impact regime, concrete material properties are  
536 significantly sensitive to rate effect [29, 30].



537

538 Fig. 14. Rate effect on fracture energy ( $G_f$ ) of C40-1 specimens

539

540 **4. Parametric effect**

541 **4.1 Effect of CFRP stiffness**

542 To study the effect of CFRP stiffness on dynamic debonding properties, specimens of  
543 group C40-2 were fabricated with double-layer CFRP sheets, which doubled the  
544 stiffness ( $E_f t_f$ ) of the composite. Fig. 15 shows a comparison of the global performance  
545 and local bond properties of specimens with different CFRP stiffnesses. The global  
546 performance of these shear tests includes ultimate load and ultimate displacement. The  
547 local bond properties are the key parameters which dominate local debonding behaviour,  
548 such as peak bond stress and fracture energy.

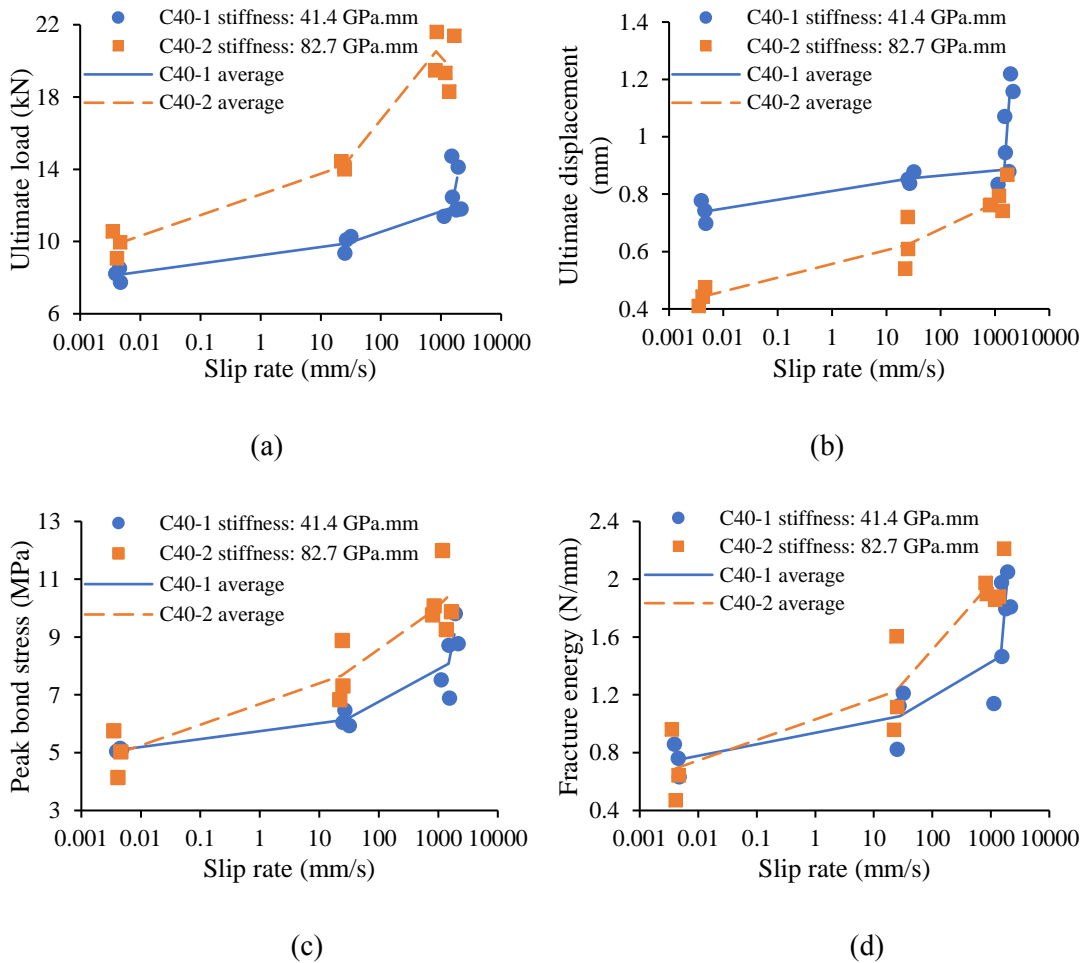


Fig. 15. Rate effect comparison between specimens of C40-1 and C40-2 for (a)

554 ultimate load, (b) ultimate displacement, (c) peak bond stress and (d) fracture energy  
555

556 Compared to C40-1 specimens, specimens of C40-2 group were generally more  
557 sensitive to slip rate, in particular, the ultimate loads of C40-2 group in Fig. 15(a)  
558 increased with a larger gradient and showed a more significant dynamic enhancing  
559 effect. Two reasons could contribute to this phenomenon. The first reason is similar to  
560 that explained for the initial stiffness shown in Fig. 13. The stiffer composite sheet could  
561 increase the initial stiffness of the bond and reduce the relative slip between the two  
562 materials. Concrete dynamic response is more sensitive to the rate effect than CFRP  
563 response [28, 30]. With a stiffer bond and less relative slip, the debonding process in  
564 C40-2 specimen is more closely linked to concrete response. Secondly, specimens in  
565 C40-2 group used a double-layer CFRP sheet which doubled the CFRP load capacity.  
566 Accordingly, specimens of C40-2 group could sustain significantly higher loading at  
567 dynamic regime. The increase of stiffness had less effect on improving dynamic peak  
568 bond stress, as shown in Fig. 15(c). Both the average curves of C40-1 and C40-2 started  
569 from about 5 MPa under quasi-static load and respectively reached 9.10 MPa and 10.37  
570 MPa at the highest rates. This phenomenon could be explained through Eq. (9). The  
571 bond stress is determined by the product of CFRP stiffness  $E_f t_f$  and strain gradient  
572  $d\varepsilon_f$ . As the strain gradients of C40-2 specimens were smaller under higher stiffness,  
573 the final bond stress did not increase significantly.

574

575 Unlike the higher values of ultimate load and peak bond stress in C40-2 group, the

576 ultimate displacements presented in Fig. 15(b) are lower than those of the control group.

577 Such performance indicated that, for the specimens with a greater CFRP stiffness,

578 concrete had more effect on the bond and the relative slip was reduced.

579

580 Among the four charts of Fig. 15, the mean ultimate displacement, peak bond stress and

581 fracture energy of samples C40-2 increased moderately at a slip rate above 1000 mm/s.

582 The average ultimate load even decreased slightly in this range. Such a phenomenon

583 could be due to scattering of test results at high slip rates.

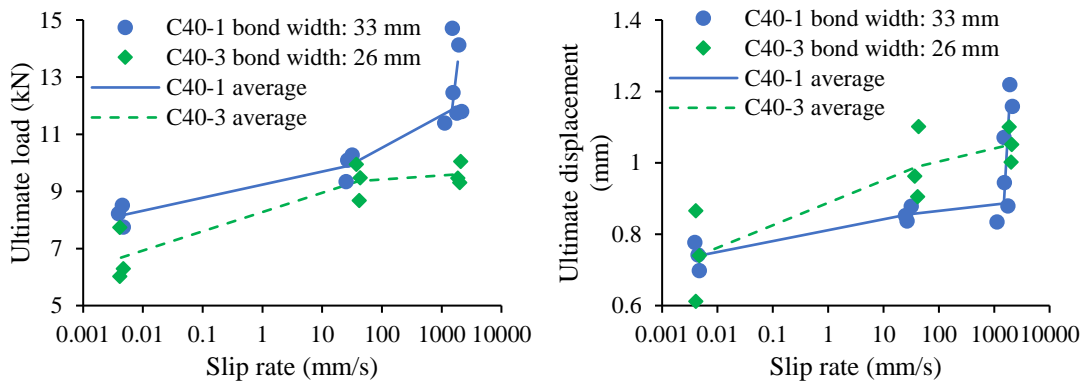
584

#### 585 4.2 Effect of CFRP-concrete bond width ratio

586 Specimens of C40-3 used CFRP sheets with a width of 26 mm, narrower than the 33

587 mm sheets used for other samples. Fig. 16 presents a comparison of slip-rate effect on

588 these narrower samples and on control group C40-1.

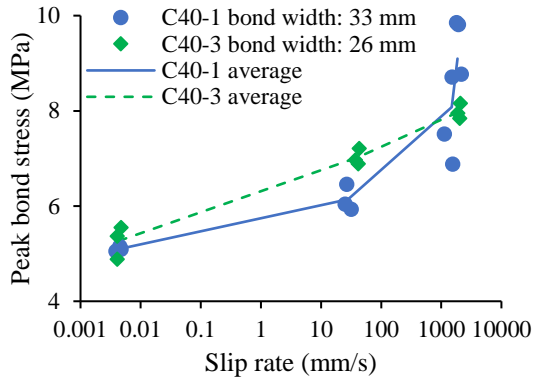


589

(a)

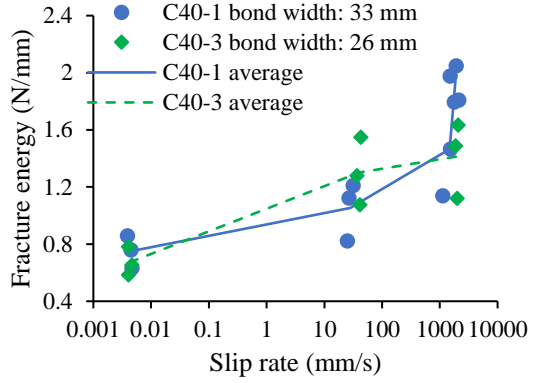
(b)

590



591

(c)



(d)

592

593 Fig. 16. Rate effect comparison between specimens of C40-1 and C40-3 on (a)

594 ultimate load, (b) ultimate displacement, (c) peak bond stress and (d) fracture energy

595

596 The dynamic increase in mechanical properties of samples C40-3 is seen in Fig. 16.

597 Due to the narrower bond width of CFRP, the ultimate loads were lower than those of

598 C40-1. However, the mean ultimate displacement values were greater than those of the

599 control group, except for the final set at the highest slip rate. Since the CFRP stiffness

600 of the two sample types was the same, the larger deformations in specimens with the

601 narrower CFRP sheets indicated higher axial stresses than those in the control group at

602 equal slip rates. Beyond a slip rate of 40 mm/s, unlike the remarkable increases of C40-

603 1, the ultimate load and the ultimate displacement of samples C40-3 increased

604 moderately. This difference could be caused by the dynamic loads in the high slip rate

605 region approaching the CFRP maximum load of 9.75 kN, as explained in Section 3.2.

606

607 In Figs. 16(c) and 16(d), under quasi-static load, the peak bond stress and fracture

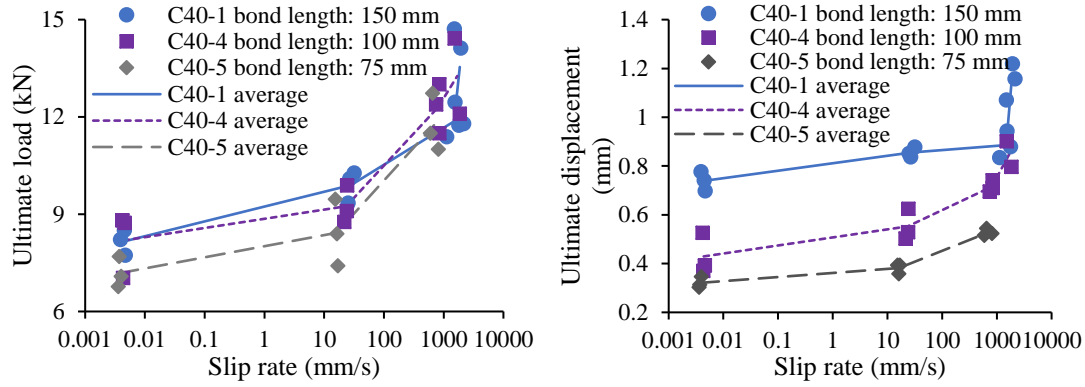
608 energy of the two groups were similar. At a slip rate of 40 mm/s, the bond properties of

609 C40-3 specimens were slightly higher than those of control group. Observing the failure  
610 behaviour of the specimens after the tests, it was found that composite debonding  
611 failure was not only located in the concrete below the bonding area, but also extended  
612 to nearby concrete. Therefore, the narrow sheets could reach a higher mobilised  
613 concrete-to-CFRP width ratios, which meant more concrete contributing to the  
614 debonding capacity for a unit width of CFRP sheet. This finding could explain the  
615 slightly higher peak bond stresses and fracture energies in group C40-3. At a slip rate  
616 of around 2000 mm/s, both values of peak bond stress and fracture energy of group  
617 C40-3 were lower than those of C40-1. As mentioned in Section 3.2, the limitation of  
618 CFRP maximum load in C40-3 group restricted further development of dynamic  
619 enhancing effect on this group. The specimen S1-C40-3A even failed by CFRP fracture.

620

#### 621 **4.3 Effect of bond length**

622 The effect of bond length was studied with specimens C40-4 and C40-5, which used  
623 CFRP sheets with lengths of 100 mm and 75 mm, respectively. Fig. 17 presents a  
624 comparison of the slip-rate effect on ultimate load and ultimate displacement between  
625 these specimens and the control group of C40-1. Due to a shorter bond length of 100  
626 mm or 75 mm compared to 150 mm, it was not able to obtain complete bond stress-slip  
627 curves for analysis of local properties from the results of C40-4 and C40-5. Therefore,  
628 the effect of bond length on the peak bond stress and fracture energy is not presented in  
629 this section.



630

631

(a)

(b)

632 Fig. 17. Rate effect comparison between specimens of C40-1, C40-4 and C40-5 on (a)

633

ultimate load and (b) ultimate displacement

634

635 In Fig. 17(a), the average values of the ultimate load of samples C40-4 were close to

636 those of group C40-1 under all slip rates. Instead, due to their shorter bond length, the

637 average values of C40-5 specimens were lower under low slip rates. As measured in

638 the quasi-static tests, the effective bond lengths of samples C40-1 and C40-4 were

639 around 90 mm. The actual CFRP bond lengths of these samples were longer than the

640 effective bond length and this guaranteed that their ultimate loads would be fully

641 developed. However, the shorter length of C40-5 specimens restricted the full

642 development of ultimate load. According to the results, the effect of bond length under

643 low slip rate was similar to the quasi-static scenario. However, at a high slip rate of 689

644 mm/s, the ultimate load for the C40-5 group significantly increased and attained the

645 values of the other two groups. This increase in the ultimate load could be attributed to

646 an increase of concrete strength under a high slip rate. Based on Eq. (5), the effective

647 bond length is inversely proportional to concrete strength. Due to the dynamic increase

648 of concrete strength at a high slip rate, the effective bond length should be shorter than  
 649 that for a lower slip rate. The equal load-carrying capacity of samples of C40-5 and  
 650 C40-1 at high slip rates verified this trend.

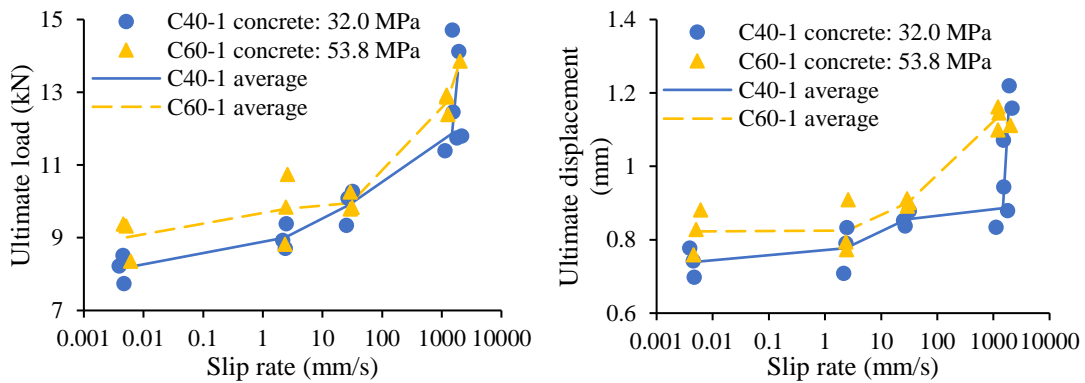
651

652 In Fig. 17(b), the general behaviour of ultimate displacement among all three sets was  
 653 an increase with growing slip rate. The ultimate displacement values consistently  
 654 reduced with shorter bond length.

655

656 **4.4 Effect of concrete strength**

657 The specimens of group C60-1 had concrete cylinder strength of 53.8 MPa. Fig. 18  
 658 presents a comparison of the results for C60-1 specimens and control group C40-1.

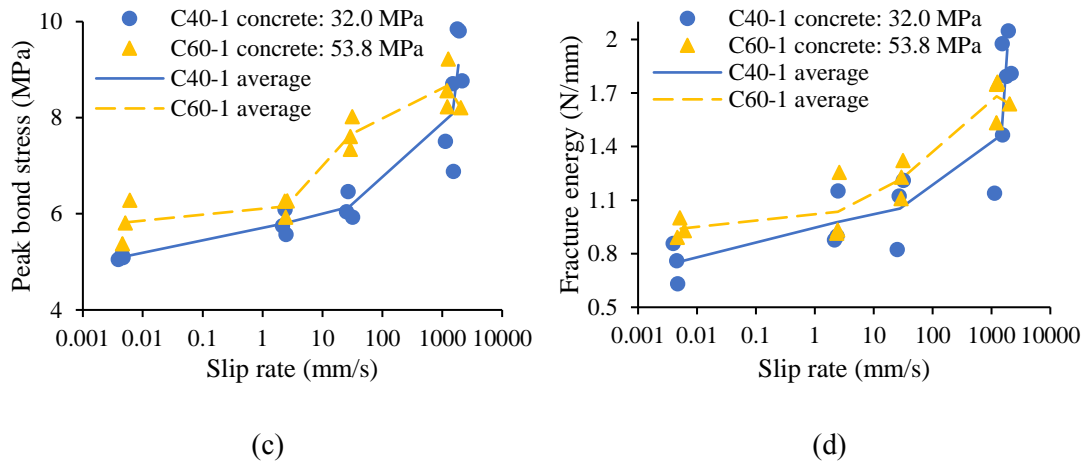


659

(a)

(b)

661



662

663

664 Fig. 18. Rate effect comparison between specimens of groups C40-1 and C60-1 on (a)

665 ultimate load, (b) ultimate displacement, (c) peak bond stress and (d) fracture energy

666

667 Among the four charts of Fig. 18, due to higher concrete strength, the results for

668 specimens of C60-1 group were all higher in the quasi-static tests. However, as slip rate

669 increased to 30 mm/s, the gap between the two groups generally reduced, as shown in

670 Figs. 18(a), 18(b) and 18(d). At the high slip rates above 1000 mm/s, the test results of

671 both groups grew rapidly in the four charts, but the test results C60-1 were caught up

672 by the control group of C40-1. In Fig. 18(c), the behaviour of the peak bond stress of

673 C60-1 was similar to its behaviour in the other three figures, except for the significant

674 increase at a rate of 30 mm/s. Therefore, the general dynamic enhancement of the C60-

675 1 specimens was lower than that seen for control group. Due to higher ultimate loads

676 of C60-1 specimens under low slip rates, the corresponding axial loads in CFRP sheets

677 were higher than those of C40-1 specimens, which resulted in a lower residual capacity

678 for dynamic response before reaching the CFRP maximum load. This limit could also

679 be seen in tests at slip rates above 1000 mm/s. The dynamic load values reached the

680 CFRP maximum load and resulted in fracture failure of CFRP sheets of specimens S2-  
681 C60-1B and C, identical to the scenario shown in Fig. 7(d).

682

683 From the experimental study, parametric effect on the bond interface is understood as  
684 follows. CFRP sheet with high stiffness could result in a stiffer bond and reduce the  
685 relative slip between CFRP and concrete. The CFRP sheet with a lower load capacity  
686 was observed by fracture failure in the sheet itself in the modified SHPB tests. However,  
687 a larger CFRP load capacity in C40-2 group could make the bond sustain a significant  
688 dynamic loading at the impact regime. In the comparison of specimens with different  
689 bond lengths, effective bond length was found to decrease due to the increase of  
690 concrete strength at a high slip rate. From the comparison of different concrete strengths,  
691 concrete of higher strength could make the bond less sensitive to dynamic enhancing  
692 effect.

693

## 694 **5. Constitutive equations for dynamic bond-slip behaviour**

695 The bond-slip behaviour is essential in studies of FRP-strengthened concrete structures  
696 [3, 13]. Considering the application in the structural analysis with dynamic loading,  
697 constitutive equations are proposed here to describe the dynamic bond-slip behaviour.  
698 As the bond-slip models proposed by Lu et al. [3] have been validated in quasi-static  
699 analysis in Section 3.1, the constitutive equations in the current study are based on their  
700 quasi-static models and dynamic increase factor (DIF) equations proposed in this paper.  
701 Two types of models are proposed for the dynamic bond-slip behaviour, including one

702 model with exponential softening law for accurate simulation and the other bilinear  
 703 model for simplified modelling.

704

705 The dynamic bond-slip model with exponential softening law is shown as:

$$706 \quad \tau = \begin{cases} ks, & \text{if } s \leq s_{0d} \\ \tau_d \cdot e^{-\alpha(\frac{s}{s_{0d}}-1)}, & \text{if } s > s_{0d} \end{cases} \quad (11)$$

707 where initial stiffness  $k$  is given by  $k = \frac{\tau_{st}}{s_0}$ , quasi-static peak bond stress  $\tau_{st}$  is given

708 by Eq. (1), slip corresponding to quasi-static peak bond stress  $s_0 = 0.0195\beta_w f_t$ ,  $\alpha =$

709  $\frac{1}{\frac{G_{fd}}{\tau_d s_{0d}} - 2}$ . Dynamic peak bond stress  $\tau_d$  and its corresponding slip  $s_{0d}$  are determined

710 by

$$711 \quad \tau_d = DIF_\tau \cdot \tau_{st} \quad (12)$$

$$712 \quad s_{0d} = \frac{\tau_d}{k} \quad (13)$$

713 where  $DIF_\tau$  is DIF of peak bond stress under different slip rate.

714

715 Dynamic fracture energy  $G_{fd}$  is determined by

$$716 \quad G_{fd} = DIF_{Gf} \cdot G_{fst} \quad (14)$$

717 where quasi-static fracture energy  $G_{fst}$  is given by Eq. (2),  $DIF_{Gf}$  is DIF of fracture

718 energy under different slip rate.

719

720 The bilinear bond-slip model is a simplified model which is widely used in structural

721 analysis of FRP strengthened concrete structures [3, 21]. The dynamic bilinear model

722 is written as:

723 
$$\tau = \begin{cases} ks, & \text{if } s \leq s_{0d} \\ \tau_d \frac{s_f - s}{s_f - s_{0d}}, & \text{if } s_{0d} < s \leq s_f \end{cases} \quad (15)$$

724 where ultimate slip  $s_f = 2G_{fd}/\tau_d$ .

725

726 According to the analyses of test results presented in Sections 3 and 4 of this paper, the  
 727 dynamic bond behaviour of the FRP-concrete interface is close to the dynamic response  
 728 of concrete material and is further affected by CFRP material parameters. The power  
 729 function given by CEB-FIP Model Code 1990 [30] is used to determine the DIF of  
 730 concrete material. As the dynamic response of the bond is close to that of concrete  
 731 material, analogous power functions are used for the DIF of the peak bond stress ( $\tau_d$ )  
 732 and the fracture energy ( $G_{fd}$ ), as shown in Eq. (16.1) and Eq. (17.1), respectively. In  
 733 the analysis of the test results in this paper, the best-fit coefficients  $a$  and  $b$  in these  
 734 equations are determined by concrete cylinder strength ( $f'_c$ ) and CFRP load capacity  
 735 ( $P_f$ ), as shown in Eq. (16.2) and Eq. (17.2). The prediction curves of both DIF equations  
 736 are presented in Fig. 19.

737 
$$DIF_{\tau} = \left(\frac{\dot{s}}{\dot{s}_0}\right)^a \quad (16.1)$$

738 where the best-fit coefficient  $a$  is

739 
$$a = 0.0334 * \ln\left(\frac{P_f/P_0}{f'_c/f_0}\right) - 0.0135 \quad (16.2)$$

740 where  $\dot{s}_0 = 0.004$  mm/s is regarded as the slip rate for quasi-static load,  $P_f$  is the load  
 741 capacity of CFRP sheet,  $P_0 = 1$  kN,  $f'_c$  is the cylinder concrete strength,  $f_0 = 10$  MPa.  
 742 As the current study tested specimens with 100 mm wide concrete substrate, the  
 743 predictions with other widths of concrete substrate could be assumed to follow the

744 equivalent width ratio as  $\frac{b_{f0}}{b_{c0}} = \frac{b_{f-real}}{b_{c-real}}$ , where  $b_{f-real}$  and  $b_{c-real}$  are real width  
 745 values of CFRP and concrete,  $b_{c0}=100$  mm,  $b_{f0}$  is an equivalent CFRP bond width.  
 746 Therefore, for those cases with different widths of concrete and CFRP sheet, the CFRP  
 747 load capacity can be determined by an equivalent maximum load of  $P_f = f_{tf} t_f b_{f0}$ ,  
 748 where  $f_{tf}$  is CFRP tensile strength.

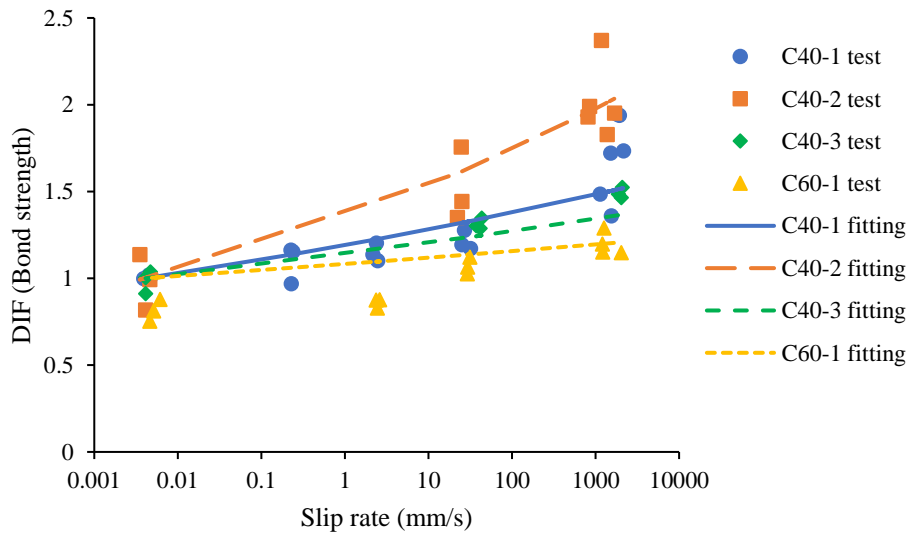
749

750 The DIF equation for dynamic fracture energy is shown as

751 
$$DIF_{Gf} = \left(\frac{\dot{s}}{\dot{s}_0}\right)^b \tag{17.1}$$

752 where the best-fit coefficient  $b$  is

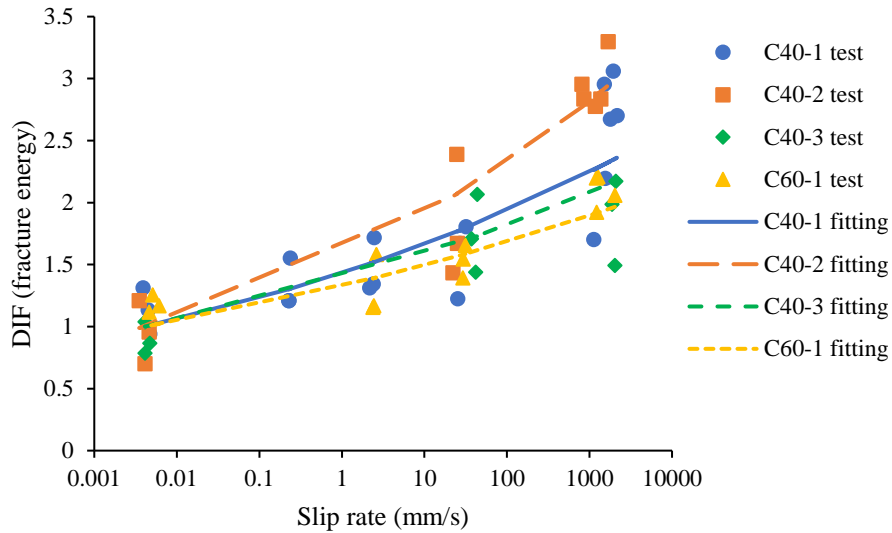
753 
$$b = 0.0264 * \ln\left(\frac{P_f/P_0}{f'_c/f_0}\right) + 0.0295 \tag{17.2}$$



754

755

(a)



(b)

Fig. 19. DIF of (a) the peak bond stress and (b) the fracture energy

756

757

758

759

760 The dynamic bond-slip curves predicted by the exponential law and the bilinear law are

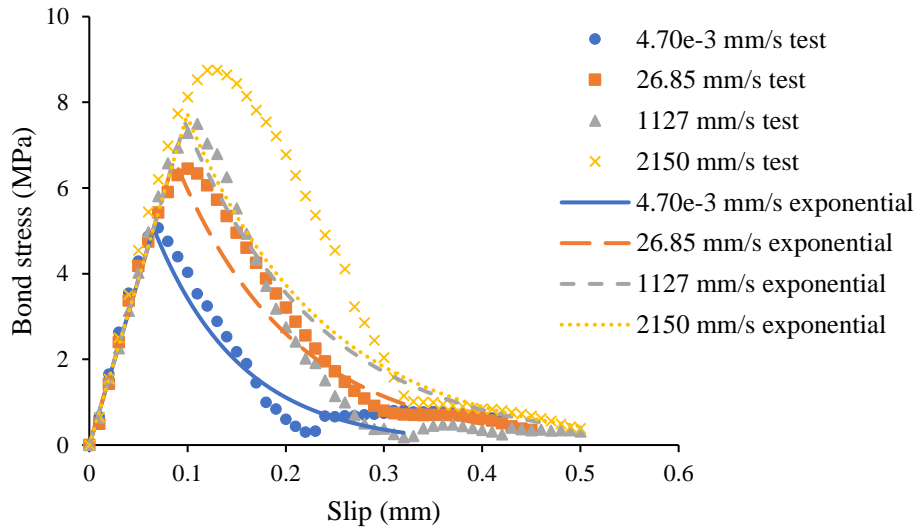
761 presented in Figs. 20(a) and 20(b), respectively. Compared with test results of C40-1

762 specimens, both models reasonably predicted the ascending and descending ranges of

763 the bond-slip curves in the slip rate range from  $4.70 \times 10^{-3}$  mm/s to 2150 mm/s. Therefore,

764 both models could be further used in structural analysis of CFRP strengthened RC

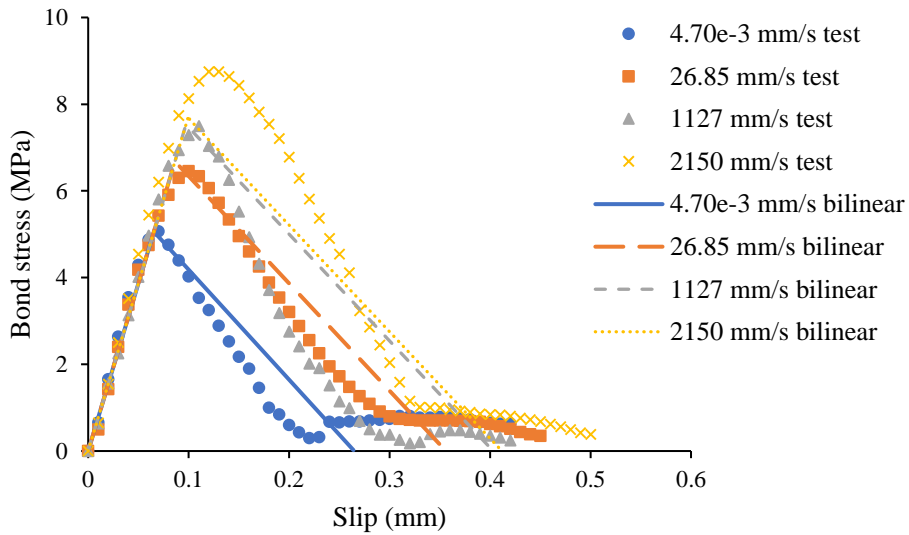
765 structures subjected to blast loading.



766

767

(a)



768

769

(b)

770 Fig. 20. Predicted dynamic bond-slip curves of C40-1 specimens by (a) the

771

exponential model and (b) the bilinear model

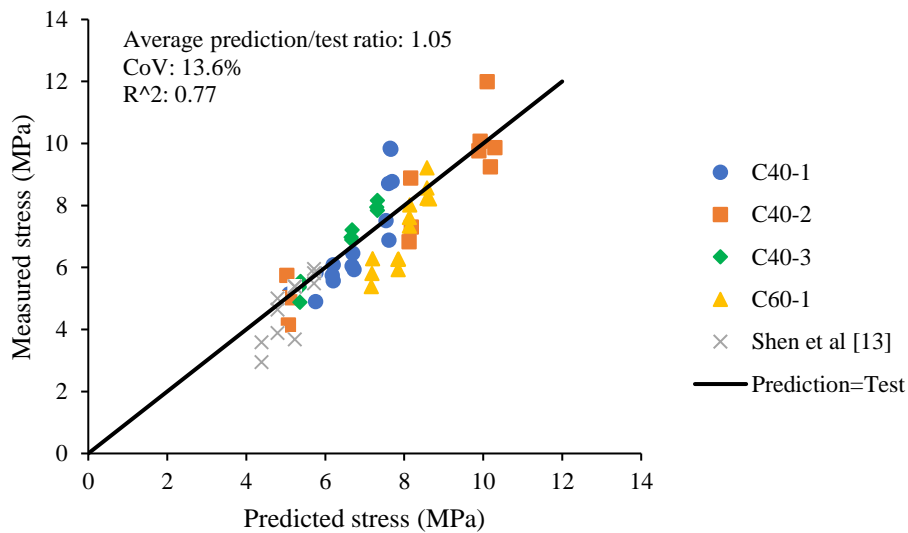
772

773 To further verify the applicability of these DIF equations with different types of FRP,

774 these equations were used to predict results of dynamic double-lap shear tests

775 conducted by Shen et al. [13]. These tests used basalt fibre reinforced polymer (BFRP)

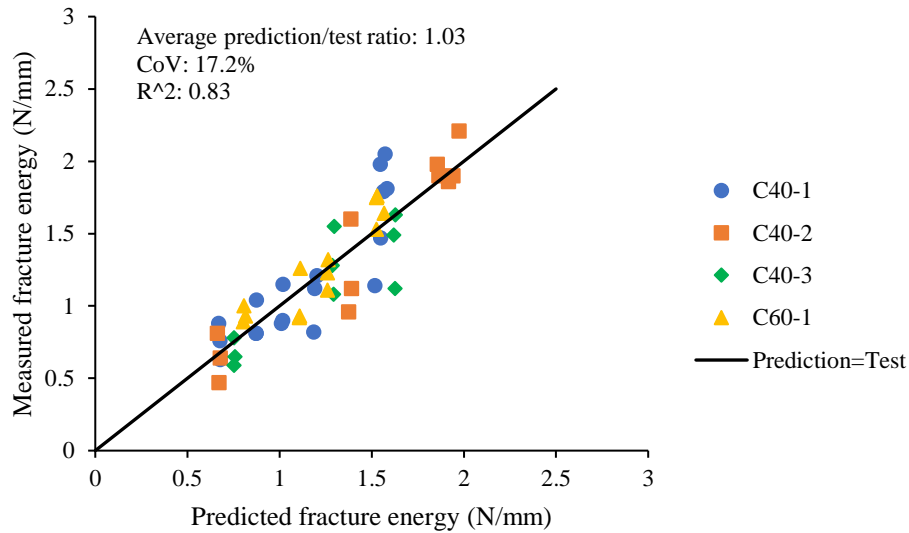
776 and a higher FRP-concrete width ratio of 0.5. The material and geometric properties of  
 777 their specimens were as follows:  $f'_c=29.6$  MPa,  $b_c=100$  mm,  $f_{tf}=2300$  MPa,  $E_f=105$   
 778 GPa,  $t_f=0.121$  mm and  $b_f=50$  mm. Fig. 21 shows that the proposed DIF equations  
 779 accurately predicted the fifty-one test results of this study and twelve experiments by  
 780 Shen et al. [13], with acceptable mean prediction-to-test ratios of peak bond stress,  
 781 fracture energy and ultimate load. Corresponding coefficients of variations (CoV) vary  
 782 between 9.0% and 17.2%.  $R^2$  falling between 0.77 and 0.89 is considered reasonable  
 783 taking into account the nature of these materials and tests [15].



784

785

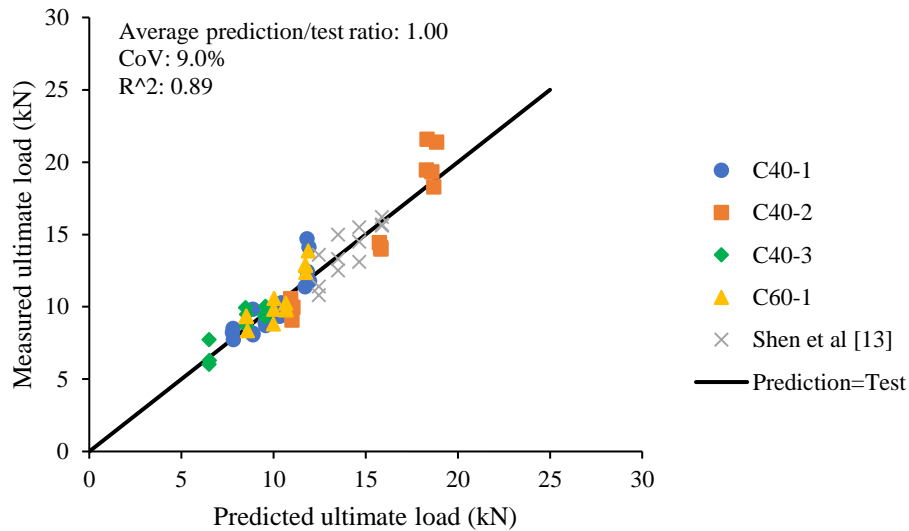
(a) peak bond stress



786

787

(b) fracture energy



788

789

(c) ultimate load

790

Fig. 21. Comparison of DIF predicted values with test results

791

792 The DIF equations were validated for specimens with a concrete strength in the range  
 793 of 30 to 55 MPa. For specimens with a higher concrete strength of over 55 MPa, the  
 794 dynamic debonding behaviour should be still influenced by the CFRP load capacity and  
 795 concrete strength. The corresponding dynamic bond properties could be predicted

796 through the proposed DIF equations. It would be better if the predictions could be  
797 validated by actual test results in future.

798

## 799 **6. Conclusion**

800 In this study, 75 specimens were tested to investigate the dynamic enhancing effect on  
801 the interfacial bond-slip behaviour from quasi-static to high slip rates (0.004 mm/s to  
802 about 2000 mm/s). To achieve the high slip rate of 2000 mm/s, the authors proposed a  
803 novel experimental method with a modified SHPB set-up. A gripping system was added  
804 to clamp the CFRP sheet and spread the impact load from the incident bar. A high-  
805 frequency data logger was used to record strain data along the CFRP bond length. The  
806 test results and failure modes were analysed to gain understanding of the bond  
807 behaviour between CFRP and concrete structures. Debonding failure in concrete layer  
808 was observed for all quasi-static tests and most of dynamic tests. Additionally,  
809 debonding failure could also occur in both concrete and epoxy due to stress  
810 concentration under dynamic loading. However, at a significant high slip rate, the  
811 dynamic ultimate load could reach CFRP load capacity and the failure mode would  
812 switch from CFRP debonding from concrete substrate to CFRP fracture. Such a failure  
813 mode under high slip rate indicated that the bond strength could be limited by the CFRP  
814 load capacity.

815

816 In the analysis of interface bond behaviour, it was clearly found that, with an increase  
817 of slip rate, the bond properties including the ultimate loads, the ultimate displacement,

818 the peak bond stress and the fracture energy increased significantly. Since the relative  
819 slip between the two materials spread the load from CFRP to concrete, the dynamic  
820 behaviour of the interface bond is closely related to concrete dynamic response.

821

822 Through this experimental study, a better understanding of the influence of CFRP  
823 stiffness, CFRP bond width and bond length, and concrete strength on the bond  
824 behaviour was achieved. Increasing the CFRP stiffness could result in a stiffer bond and  
825 reduce the relative slip between CFRP and concrete. When the effect of CFRP bond  
826 width was studied, it was found that CFRP width directly affected CFRP load capacity.

827 At the impact regime, a lower CFRP load capacity could lead to the failure mode of  
828 CFRP fracture rather than debonding from concrete substrate. In this way, the interface  
829 bond could not withstand violent impact and CFRP sheet could not provide further  
830 protection for concrete structures. However, in the same regime, the CFRP-concrete  
831 bond joint with a higher CFRP load capacity could sustain a significant dynamic  
832 loading. In terms of CFRP bond length, reducing the length below the effective bond  
833 length could decrease the ultimate load and ultimate displacement of the specimens at  
834 a low slip rate. However, at a high slip rate, specimens with a much shorter bond length  
835 could attain equal ultimate loads as those specimens with longer bond length. This  
836 phenomenon indicated that effective bond length would reduce due to dynamic increase  
837 of concrete strength. From the comparison of specimens with different concrete  
838 strengths, higher strength concrete could make the ultimate loads of the single-lap shear  
839 tests approach CFRP load capacity and result in the bond-slip behaviour becoming less

840 sensitive to dynamic enhancing effect.

841

842 The constitutive equations were proposed for the dynamic bond-slip behaviour and  
843 their accuracy was determined through a comparison with the obtained experimental  
844 results. The average prediction-to-test ratios of peak bond stress, fracture energy and  
845 ultimate load ranged from 1.00 to 1.05, with CoVs below 17.2%. These equations can  
846 be used to define the mechanical behaviour for the CFRP-concrete interface in dynamic  
847 structural analysis. It should be noted that the scope of the DIF equations is limited to  
848 a concrete strength below 55 MPa and a CFRP load capacity below 25 kN. Further  
849 study of the dynamic interfacial properties is recommended for specimens with high  
850 strength concrete (over 55 MPa) and a higher CFRP load capacity. Moreover, concrete-  
851 metal interface bond is widely found for concrete-steel composite structures. The  
852 dynamic debonding behaviour of concrete-metal interface bond is worth further study.

853

#### 854 **Acknowledgement**

855 The authors acknowledge the research scholarship given by Nanyang Technological  
856 University and the research grant of the project “Modelling of Fibre-Reinforced  
857 Polymer (FRP) Strengthened Reinforced Concrete Walls subject to Blast and Fragment  
858 Loadings” from the Defence Science and Technology Agency (DSTA), Singapore. The  
859 authors are grateful for their support in this research.

860

861 **Reference**

- 862 1. Yao, J., Teng, J., and Chen, J.F., *Experimental study on FRP-to-concrete bonded*  
863 *joints*. Composites Part B: Engineering, 2005. **36**(2): p. 99-113.
- 864 2. Chen, J.F. and Teng, J., *Anchorage strength models for FRP and steel plates*  
865 *bonded to concrete*. Journal of Structural Engineering, 2001. **127**(7): p. 784-791.
- 866 3. Lu, X., Teng, J., Ye, L., and Jiang, J., *Bond–slip models for FRP sheets/plates*  
867 *bonded to concrete*. Engineering structures, 2005. **27**(6): p. 920-937.
- 868 4. Dai, J., Ueda, T., and Sato, Y., *Development of the nonlinear bond stress–slip*  
869 *model of fiber reinforced plastics sheet–concrete interfaces with a simple*  
870 *method*. Journal of Composites for Construction, 2005. **9**(1): p. 52-62.
- 871 5. Cottone, A. and Giambanco, G., *Minimum bond length and size effects in FRP–*  
872 *substrate bonded joints*. Engineering Fracture Mechanics, 2009. **76**(13): p.  
873 1957-1976.
- 874 6. Shi, J.-W., Cao, W.-H., and Wu, Z.-S., *Effect of adhesive properties on the bond*  
875 *behaviour of externally bonded FRP-to-concrete joints*. Composites Part B:  
876 Engineering, 2019. **177**: p. 107365.
- 877 7. La Malfa Ribolla, E., Rezaee Hajidehi, M., Rizzo, P., Fileccia Scimemi, G.,  
878 Spada, A., and Giambanco, G., *Ultrasonic inspection for the detection of*  
879 *debonding in CFRP-reinforced concrete*. Structure and Infrastructure  
880 Engineering, 2018. **14**(6): p. 807-816.
- 881 8. Orton, S.L., Chiarito, V.P., Minor, J.K., and Coleman, T.G., *Experimental testing*  
882 *of CFRP-strengthened reinforced concrete slab elements loaded by close-in*  
883 *blast*. Journal of Structural Engineering, 2013. **140**(2): p. 04013060.
- 884 9. Muszynski, L.C. and Purcell, M.R., *Use of composite reinforcement to*  
885 *strengthen concrete and air-entrained concrete masonry walls against air blast*.  
886 Journal of Composites for Construction, 2003. **7**(2): p. 98-108.
- 887 10. Tanapornraweekit, G., Haritos, N., and Mendis, P., *Behavior of FRP-RC slabs*  
888 *under multiple independent air blasts*. Journal of Performance of Constructed  
889 Facilities, 2010. **25**(5): p. 433-440.
- 890 11. Orton, S.L., Chiarito, V.P., Rabalais, C., Wombacher, M., and Rowell, S.P.,  
891 *Strain rate effects in CFRP used for blast mitigation*. Polymers, 2014. **6**(4): p.  
892 1026-1039.
- 893 12. Shi, J., Zhu, H., Wu, Z.S., and Diab, H. *Strain rate effect on the bond of FRP*  
894 *laminated concrete interface*. in *International Conference on Fiber Reinforced*  
895 *Polymer (FRP) Composites in Civil Engineering 2012*. CICE.
- 896 13. Shen, D., Shi, X., Ji, Y., and Yin, F., *Strain rate effect on bond stress-slip*  
897 *relationship between basalt fiber-reinforced polymer sheet and concrete*.  
898 Journal of Reinforced Plastics and Composites, 2015. **34**(7): p. 547-563.
- 899 14. Caggiano, A., Martinelli, E., Schicchi, D.S., and Etse, G., *A modified Duvaut-*  
900 *Lions zero-thickness interface model for simulating the rate-dependent bond*  
901 *behavior of FRP-concrete joints*. Composites Part B: Engineering, 2018. **149**:  
902 p. 260-267.
- 903 15. Pereira, J.M. and Lourenço, P.B., *Experimental bond behaviour of GFRP and*

- 904 *masonry bricks under impulsive loading*. Materials and Structures, 2016. **49**(11):  
905 p. 4799-4811.
- 906 16. Li, X., *FRP-to-concrete bond behaviour under high strain rates*, in *Doctor*  
907 *thesis*. 2012, The University of Edinburgh.
- 908 17. Marzi, S., Hesebeck, O., Brede, M., and Kleiner, F. *A rate-dependent, elasto-*  
909 *plastic cohesive zone mixed-mode model for crash analysis of adhesively*  
910 *bonded joints*. in *7th European LS-DYNA conference*. 2009.
- 911 18. Nitowrap, F., *High strength carbon fibre sheet wrap system for structural*  
912 *reinforcement*, in *Fosroc*.
- 913 19. Standard, A., *D3039/D3039M-00*. Standard test method for tensile properties of  
914 polymer matrix composite materials, 2000.
- 915 20. Zhou, Y., Xia, K.-w., Li, X., Li, H., Ma, G., Zhao, J., Zhou, Z., and Dai, F.,  
916 *Suggested methods for determining the dynamic strength parameters and mode-*  
917 *I fracture toughness of rock materials*. International Journal of Rock Mechanics  
918 and Mining Sciences, 2012. **49**: p. 105-112.
- 919 21. Yuan, H., Teng, J., Seracino, R., Wu, Z., and Yao, J., *Full-range behavior of*  
920 *FRP-to-concrete bonded joints*. Engineering Structures, 2004. **26**(5): p. 553-565.
- 921 22. Wu, Z., Yuan, H., and Niu, H., *Stress transfer and fracture propagation in*  
922 *different kinds of adhesive joints*. Journal of Engineering Mechanics, 2002.  
923 **128**(5): p. 562-573.
- 924 23. Du Béton, F.I., *Externally bonded FRP reinforcement for RC structures*.  
925 Bulletin, 2001. **14**: p. 138.
- 926 24. Ueda, T. and Dai, J., *Interface bond between FRP sheets and concrete substrates:*  
927 *properties, numerical modeling and roles in member behaviour*. Progress in  
928 Structural Engineering and Materials, 2005. **7**(1): p. 27-43.
- 929 25. Nakaba, K., Kanakubo, T., Furuta, T., and Yoshizawa, H., *Bond behavior*  
930 *between fiber-reinforced polymer laminates and concrete*. Structural Journal,  
931 2001. **98**(3): p. 359-367.
- 932 26. Lee, Y., Boothby, T., Bakis, C., and Nanni, A., *Slip modulus of FRP sheets*  
933 *bonded to concrete*. Journal of Composites for Construction, 1999. **3**(4): p. 161-  
934 167.
- 935 27. Mutalib, A.A. and Hao, H., *Numerical Analysis of FRP-Composite-*  
936 *Strengthened RC Panels with Anchorages against Blast Loads*. Journal of  
937 Performance of Constructed Facilities, 2011. **25**(5): p. 360-372.
- 938 28. Zhang, X., Hao, H., Shi, Y., Cui, J., and Zhang, X., *Static and dynamic material*  
939 *properties of CFRP/epoxy laminates*. Construction and Building Materials,  
940 2016. **114**: p. 638-649.
- 941 29. Lukić, B.B., Saletti, D., and Forquin, P., *On the processing of spalling*  
942 *experiments. Part II: Identification of concrete Fracture Energy in dynamic*  
943 *tension*. Journal of Dynamic Behavior of Materials, 2018. **4**(1): p. 56-73.
- 944 30. CEB-FIP, *Model code for concrete structures 90*. 1993, Thomas Telford Ltd.,  
945 London, UK.

946